

# Intrinsic H<sup>+</sup> ion mobility in the rabbit ventricular myocyte

R. D. Vaughan-Jones\*, B. E. Peercy†, J. P. Keener† and K. W. Spitzer‡

\* University Laboratory of Physiology, Parks Road, Oxford OX1 3PT, UK, † Nora Eccles Harrison Cardiovascular Research and Training Institute and ‡ Department of Mathematics, University of Utah, Salt Lake City, UT, USA

The intrinsic mobility of intracellular H<sup>+</sup> ions was investigated by confocally imaging the longitudinal movement of acid inside rabbit ventricular myocytes loaded with the acetoxymethyl ester (AM) form of carboxy-seminaphthorhodafluor-1 (carboxy-SNARF-1). Acid was diffused into one end of the cell through a patch pipette filled with an isotonic KCl solution of pH 3.0. Intracellular H<sup>+</sup> mobility was low, acid taking 20–30 s to move 40 μm down the cell. Inhibiting sarcolemmal Na<sup>+</sup>–H<sup>+</sup> exchange with 1 mM amiloride had no effect on this time delay. Net H<sub>i</sub><sup>+</sup> movement was associated with a longitudinal intracellular pH (pH<sub>i</sub>) gradient of up to 0.4 pH units. H<sub>i</sub><sup>+</sup> movement could be modelled using the equations for diffusion, assuming an apparent diffusion coefficient for H<sup>+</sup> ions ( $D_{app}^H$ ) of  $3.78 \times 10^{-7} \text{ cm}^2 \text{ s}^{-1}$ , a value more than 300-fold lower than the H<sup>+</sup> diffusion coefficient in a dilute, unbuffered solution. Measurement of the intracellular concentration of SNARF (~400 μM) and its intracellular diffusion coefficient ( $0.9 \times 10^{-7} \text{ cm}^2 \text{ s}^{-1}$ ) indicated that the fluorophore itself exerted an insignificant effect (between 0.6 and 3.3 %) on the longitudinal movement of H<sup>+</sup> equivalents inside the cell. The longitudinal movement of intracellular H<sup>+</sup> is discussed in terms of a diffusive shuttling of H<sup>+</sup> equivalents on high capacity mobile buffers which comprise about half (~11 mM) of the total intrinsic buffering capacity within the myocyte (the other half being fixed buffer sites on low mobility, intracellular proteins). Intrinsic H<sub>i</sub><sup>+</sup> mobility is consistent with an average diffusion coefficient for the intracellular mobile buffers ( $D_{mob}$ ) of  $\sim 9 \times 10^{-7} \text{ cm}^2 \text{ s}^{-1}$ .

(Received 10 September 2001; accepted after revision 8 February 2002)

**Corresponding author** R. D. Vaughan-Jones: University Laboratory of Physiology, Parks Road, Oxford OX1 3PT, UK.  
Email: richard.vaughan-jones@physiol.ox.ac.uk

Intracellular pH (pH<sub>i</sub>) is an important modulator of cell function. In the heart, pH<sub>i</sub> influences contractility (Vaughan-Jones *et al.* 1987; Bountra & Vaughan-Jones, 1989; Kohmoto *et al.* 1990; Harrison *et al.* 1992) and can affect the generation of arrhythmias (Orchard & Cingolani, 1994; Ch'en *et al.* 1998). Intracellular pH is regulated by acid-equivalent transporters expressed at the sarcolemma (Leem *et al.* 1999). It is usually assumed that these communicate with a cytoplasmic compartment that is spatially uniform with respect to the distribution of H<sup>+</sup> ions. Recent work, however, is challenging this view. In the duodenal enterocyte (an epithelial cell) significant spatial non-uniformity of cytoplasmic pH occurs during activation of apical acid transport (Stewart *et al.* 2000). Spatial gradients of pH<sub>i</sub> can also be induced in cultured enterocyte monolayers (Gonda *et al.* 1999) and in acutely isolated cardiac myocytes (Spitzer *et al.* 2000) by applying weak acids or bases (such as CO<sub>2</sub> or NH<sub>3</sub>) to localized regions of the surface membrane.

The most likely explanation for the occurrence of pH<sub>i</sub> gradients is that the effective, cytoplasmic mobility of the H<sup>+</sup> ion (or its ionic equivalent, such as the OH<sup>-</sup> ion) is considerably lower than its mobility in simple unbuffered solution. A rapid transmembrane flux of acid or base

would therefore be expected to cause local accumulation or depletion of H<sup>+</sup> ions in the submembranous space. The amplitude and duration of this intracellular pH microdomain would be governed by the effective rate of diffusion of H<sup>+</sup> equivalents into and out of the microdomain. Given the important modulatory influence of pH<sub>i</sub>, its spatiotemporal non-uniformity may have far-reaching consequences for cell function.

In the present work we have attempted to quantify the apparent intracellular H<sup>+</sup> ion diffusion coefficient ( $D_{app}^H$ ). As will be shown, this is an empirical measure of the effective H<sup>+</sup> ion mobility, dictated by a mechanism more complex than simple, unrestricted H<sup>+</sup> diffusion. Although estimates of  $D_{app}^H$  have been reported for the duodenal enterocyte (Stewart *et al.* 2000), possible errors caused by the flux of acid across the surface membrane could not be rigorously excluded. Values have also been reported for molluscan axoplasm (Al-Baldawi & Abercrombie, 1992) but these were for extruded samples rather than for an intact cell. We have therefore investigated intracellular H<sup>+</sup> ion mobility in an intact cell where membrane acid transport has been inhibited, and for a mammalian rather than an invertebrate system. To do this, we developed a method for introducing acid into one end of an isolated

ventricular myocyte, using a cell-attached patch pipette, while observing the longitudinal movement of acid down the cell using laser scanning confocal microscopy. Intracellular pH was recorded using carboxy-seminaphthorhodafluor-1 (carboxy-SNARF-1), a pH fluorophore loaded into the cell in its acetoxymethyl ester (AM) form. As intracellular H<sup>+</sup> ion mobility may be influenced by SNARF<sub>i</sub> acting as a mobile buffer, it was also important to document the fluorophore's intracellular concentration and mobility.

Our results are presented in two papers. In this, the first paper, we examine the properties and suitability of intracellular SNARF for measuring acid-equivalent movements within ventricular myocytes, and we assess intrinsic, intracellular H<sup>+</sup> ion mobility, i.e. the effective intracellular H<sup>+</sup> equivalent mobility observed in myocytes that lack extrinsic buffer, i.e. a CO<sub>2</sub>/HCO<sub>3</sub><sup>-</sup> buffer system. Theoretical modelling (Junge & McLaughlin, 1987) plus work on extruded axoplasm (Al-Baldawi & Abercrombie, 1992) has suggested that intrinsic mobility is dictated by the mobility of intracellular, non-CO<sub>2</sub> buffers. In the accompanying paper (Spitzer *et al.* 2002) we examine the additional role played by CO<sub>2</sub>/HCO<sub>3</sub><sup>-</sup> in regulating effective H<sub>i</sub><sup>+</sup> mobility.

Preliminary accounts of some of this work have been published (Vaughan-Jones *et al.* 2000*a, b*).

## METHODS

### Cell isolation

As previously described (Skolnick *et al.* 1998), adult rabbit ventricular myocytes were obtained from New Zealand White rabbits (2–3 kg). Animals were anaesthetized with an intravenous injection of sodium pentobarbitone (50 mg kg<sup>-1</sup>) and 0.5 ml heparin to prevent clotting, in accordance with national guidelines. The heart was rapidly removed and attached to a Langendorff perfusion system. All perfusion solutions were gas equilibrated with 100% O<sub>2</sub> and held at 37°C with a pH of 7.4. Perfusion with a 0 mM Ca<sup>2+</sup> solution for 5 min was followed by 20 min of recirculation with the same solution containing 1 mg ml<sup>-1</sup> collagenase (class II, Worthington Biochemical, Freehold, NJ, USA), 0.1 mg ml<sup>-1</sup> protease (type XIV, Sigma Chemical, St Louis, MO, USA), and 0.1 mM CaCl<sub>2</sub>. The heart was then perfused for 5 min with the same solution containing no enzymes. The left ventricle was minced and shaken for 10 min and then filtered through a nylon mesh. The cells were stored at room temperature in the normal Hepes-buffered solution. All cells used in this study were rod shaped in appearance, had well-defined striations, and did not spontaneously contract. All experiments were performed within 2–5 h after isolation.

### Cell bath

Cell bathing solutions were held at 37 ± 0.1°C in glass reservoir bottles that were completely sealed except for a small vent at the top and an exit port at the bottom. Solutions were delivered by gravity from the bottles to the cell bath through thermally jacketed gas-impermeable tubing. The temperature of the solutions in the bath was 36 ± 0.3°C. The 1 ml Plexiglas cell bath had a clear glass bottom and was mounted on the stage of an inverted microscope

(Diaphot, Nikon, Japan). Hepes-buffered normal solution (for composition see below) continuously flowed through the bath at 4–6 ml min<sup>-1</sup>, and solution depth was held at approximately 3 mm. The bottom of the bath was coated with laminin (Collaborative Research, Bedford, MA, USA) to improve cell adhesion.

### Confocal measurement of pH<sub>i</sub>

The pH<sub>i</sub> was measured as previously described (Spitzer *et al.* 2000) in single myocytes using carboxy-seminaphthorhodafluor-1 (carboxy-SNARF-1) as the fluorescent pH indicator and a laser scanning confocal microscope (MRC 1024, Bio-Rad Laboratories, Hercules, CA, USA) to image the cells. Myocytes were equilibrated at 37°C for 10 min in normal Hepes solution containing 13 μM of the acetoxymethyl ester form of SNARF-1 (SNARF-AM, Molecular Probes, Eugene, OR, USA) as previously described (Spitzer & Bridge, 1992). The cells were then placed in the cell bath, where they were bathed in normal solution for at least 20 min before pH<sub>i</sub> measurements began. Excitation at 488 nm was provided by an argon-krypton mixed-gas laser (American Laser, Salt Lake City, UT, USA). Emitted fluorescence was simultaneously collected by two photomultiplier tubes equipped with band-pass filters centred at 640 ± 20 and 580 ± 20 nm via a × 40 oil-immersion objective lens (NA 1.3). A transmitted light detector also provided a non-fluorescent image of the cell. Fluorescence ratios (640 nm/580 nm) and transmitted light images were acquired on-line at a rate of ~1.5 s frame<sup>-1</sup>.

The emission ratio was calibrated as previously described (Buckler & Vaughan-Jones, 1990; Spitzer & Bridge, 1992) using solutions of varying pH that also contained nigericin. The best-fit equation for the calibration curves from several myocytes was used to calculate pH<sub>i</sub> of the cells used in this study.

Confocal images were processed using NIH Image and Transform software (Fortner Software, Sterling, VA, USA). Images were stored on recordable compact disks.

### Solutions

The nominally Ca<sup>2+</sup>-free solution used for myocyte isolation contained (mM): NaCl, 126.0; KCl, 4.4; dextrose, 22.0; MgCl<sub>2</sub>, 5.0; taurine, 20.0; creatine, 5.0; sodium pyruvate, 5.0; NaH<sub>2</sub>PO<sub>4</sub>, 1.0; Hepes, 24.0 (adjusted to pH 7.4 with 13.0 mM NaOH). The normal Hepes-buffered solution used to bathe the cells contained (mM): NaCl, 126; KCl, 4.4; MgCl<sub>2</sub>, 1.0; dextrose, 11.0; CaCl<sub>2</sub>, 1.1; Hepes, 24.0 (adjusted to pH 7.4 with 13.0 mM NaOH). In some experiments 1 mM amiloride (Sigma) was included in this solution to inhibit Na<sup>+</sup>-H<sup>+</sup> exchange.

The pipette filling solution used in most experiments to acid load myocytes contained (mM): KCl, 140; dextrose, 5.5; MgCl<sub>2</sub>, 0.5; HCl, 1.0 (pH 3). In some experiments we used a filling solution with the following composition (mM): potassium glutamate, 140; dextrose, 5.5; MgCl<sub>2</sub>, 0.5; HCl, 20.0 (pH 5).

The filling solution used to pipette load myocytes with unesterified carboxy-SNARF-1 (Molecular Probes) contained (mM): potassium glutamate, 123; dextrose, 5.5; K<sub>2</sub>ATP, 5.0; MgCl<sub>2</sub>, 1.0; Hepes, 10.0 (adjusted to pH 7.14 with 12 mM KOH). Three different concentrations of carboxy-SNARF-1 were used for pipette loading (mM): 0.105 (pH 7.11), 0.551 (pH 7.09) and 2.2 (pH 7.01). We did not compensate for the small reductions in pH of the filling solutions caused by the acidic nature of the fluorophore. These solutions were also used to determine the *in vitro* relationship between SNARF-1 fluorescence and SNARF-1 concentration ([SNARF-1]).

In some experiments we loaded carboxy-SNARF-1 into cells by permeabilizing them with digitonin. The bathing solution used for this technique contained (mM): KCl, 132.7; dextrose, 11.0; MgCl<sub>2</sub>, 1.0; Hepes, 12.0; EGTA, 1.0; nigericin, 0.013; 2,3-butanedione monoxime (BDM), 15.0; digitonin, 0.010; KOH, 7.3 (pH 7.17), and carboxy-SNARF-1, 0.276 or 0.551. In separate experiments, we found that when rabbit ventricular myocytes were loaded with SNARF-1 using SNARF-AM (13 μM) and then exposed to this high K<sup>+</sup> digitonin solution, without SNARF-1, the indicator rapidly diffused out of the cells and was undetectable by confocal imaging within 20–30 s. Immediately prior to applying the high K<sup>+</sup> digitonin solution myocytes were bathed with a zero Ca<sup>2+</sup> solution to remove extracellular Ca<sup>2+</sup>. Its composition was identical to the normal Hepes solution except it contained 1 mM EGTA and no added calcium. This procedure minimized myocyte contractures during exposure to the high K<sup>+</sup> digitonin solution. Nigericin was obtained from Sigma and digitonin from Calbiochem (La Jolla, CA, USA).

#### Pipette loading of acid and carboxy-SNARF-1

Acid was introduced into myocytes via whole-cell patch pipette attachments. The pipettes were made from borosilicate capillary glass (no. 7052, o.d. 1.65 mm, i.d. 1.20 mm, AM Systems, Inc., Everett, WA, USA). After fire polishing and filling they had electrical resistances of 1–2 MΩ. Transmembrane potential ( $V_m$ ) was monitored in bridge mode with an Axoclamp 2A amplifier system (Axon Instruments, Inc., Foster City, CA, USA) using an Ag–AgCl pellet as the reference electrode.

Cells used for pipette acid loading were previously loaded with carboxy-SNARF-1 by bath equilibration with SNARF-AM as described above. Following indicator loading they were continuously bathed with the normal Hepes solution in the absence or presence of 1 mM amiloride (pH 7.4). Confocal images of pHi in myocytes selected for study were acquired continuously before, during and after pipette attachment and break-in. Pipette attachments were made as close to the end of a cell as possible.

A similar technique was used to introduce carboxy-SNARF-1 into cells via pipettes, except in these experiments only the normal Hepes solution was used to bathe the cells.

#### In vitro determination of the relationship between SNARF-1 fluorescence and [SNARF-1]<sub>i</sub>

To determine the *in vitro* relationship between SNARF-1 fluorescence and [SNARF-1]<sub>i</sub>, solutions containing different carboxy-SNARF-1 concentrations were placed in the cell chamber. They were identical in composition to those used for pipette loading of SNARF-1. Similarly, the experimental conditions, including confocal settings and bath temperature, were identical to those used to measure pHi in SNARF-loaded cells. In contrast to unesterified SNARF, a solution containing 14 μM SNARF-AM (pH 7.1) displayed no fluorescence at either 640 or 580 nm.

#### Intracellular buffering power

When required, intrinsic intracellular buffering power ( $\beta_i$ ) was computed at a given pHi from eqn (1). This was determined experimentally by Leem *et al.* (1999) for the pHi dependence of  $\beta_i$  in the guinea pig ventricular myocyte which exhibits an intrinsic buffer capacity very similar to that of the rabbit ventricular myocyte (Skolnick *et al.* 1998):

$$\beta_i = \frac{2.3[A] \times 10^{(pH_i - pK_a)}}{(1 + 10^{(pH_i - pK_a)})^2} + \frac{2.3[B] \times 10^{(pH_i - pK_b)}}{(1 + 10^{(pH_i - pK_b)})^2}, \quad (1)$$

where A and B are two buffer populations of concentration 84.22 and 29.38 mM, respectively, and  $-\log$  of dissociation constant (pK) values (pK<sub>a</sub> and pK<sub>b</sub>) of 6.03 and 7.57, respectively.

#### Statistical analysis

Summarized results are presented as means ± S.E.M. Statistical analysis was performed using Student's *t* test for unpaired data.  $P < 0.05$  was considered significant.

## RESULTS

### Part 1. Intracellular concentration and mobility of carboxy-SNARF-1

SNARF is a weak acid with a pK of ~7.6 (Buckler & Vaughan-Jones, 1990; Blank *et al.* 1992). If it diffuses relatively freely within the cell, it will act as a mobile carrier of H<sup>+</sup> ions, thus contributing to intracellular H<sup>+</sup> ion mobility. In order to assess the extent of this phenomenon we estimated the concentration and mobility of SNARF in myocytes used for confocal pHi imaging.

#### Estimating [SNARF]<sub>i</sub>

**By matching extracellular with intracellular SNARF fluorescence.** The simplest approach to measuring [SNARF]<sub>i</sub> would be to adjust the concentration of extracellular SNARF so that, at a common pH, its fluorescence intensity matched that of the intracellular signal. This assumes that the spectral properties of SNARF are unchanged when intracellular. Figure 1A shows the fluorescence intensity of non-esterified SNARF recorded confocally (at 580 and 640 nm) in the extracellular bathing solution when different concentrations of the fluorophore were introduced into the experimental chamber. Increasing [SNARF] increased the fluorescence, but at > 1.0 mM SNARF the relationship saturated, with half-maximal intensity occurring at about 0.25 mM SNARF. Saturation is most likely to have occurred because at the higher concentrations fluorescence is quenched by neighbouring dye molecules (Haugland, 1996). Alternatively, at high dye concentration absorption of excitation light may be occurring in the out-of-plane optical path. Whatever the cause, the result is that at a given pHi increasing [SNARF] to above ~1 mM does not enhance the amplitude of the fluorescence signal.

The histogram in Fig. 1B shows average intracellular fluorescence intensity recorded confocally at 580 and 640 nm in SNARF AM-loaded myocytes (the nucleus was avoided when selecting an intracellular measurement region as this often showed a lower intensity than that of the surrounding cytoplasm, for example see Fig. 1B, right panel). Cells were selected with a resting intracellular pH of 6.99–7.10 (in order to match the pH of the extracellular medium used in Fig. 1A). Surprisingly, average intracellular fluorescence intensity (Fig. 1B) was 30–40% larger than maximal extracellular fluorescence at the same pH (cf. Fig. 1A). The simplest explanation is that the spectral properties of SNARF are altered within the cardiac cell.

The changed spectral properties of SNARF<sub>i</sub> were examined by loading the free-acid form of the dye (2.2 mM) through a cell-attached patch pipette (see Methods for solution composition), and the resulting intracellular fluorescence compared with that of an extracellular sample of the same loading solution added later to the experimental chamber (at 37 °C). The fluorescence recorded at 580 nm emission from all intracellular regions (except the nucleus) was 20–40% larger than in the extracellular sample (not

shown). A similar result was seen in two other cells. At a given pH, therefore, SNARF fluorescence intensity was higher inside myocytes irrespective of whether the dye was loaded as the AM ester or as the free acid. This means that extracellular SNARF fluorescence cannot be used to calibrate intracellular SNARF concentration.

**By permeabilizing the myocyte with digitonin.** We developed an alternative method for estimating [SNARF]<sub>i</sub>. The left panel in Fig. 2A illustrates an experiment where a SNARF-free myocyte was exposed to a high K<sup>+</sup> (140 mM) solution containing nigericin (13 μM) in order to equalize pH<sub>i</sub> to pH<sub>o</sub> (7.17). In addition, the solution contained digitonin (10 μM), to permeabilize the sarcolemma, and non-esterified SNARF (0.55 mM). Under these conditions SNARF readily crossed the sarcolemma as can be seen by the rapid appearance of intracellular fluorescence recorded at 640 and 580 nm (middle and right panels of Fig. 2A, respectively). In the absence of digitonin (not shown) no SNARF entry was detected. The ability of digitonin to permeabilize the sarcolemma to SNARF was also demonstrated by adding 10 μM digitonin to a SNARF-AM-loaded myocyte superfused with a SNARF-free solution. Under these conditions (not shown), all intracellular SNARF fluorescence was lost within 20 s.

Intracellular fluorescence intensity observed in Fig. 2A middle and right panels is greater than in the bathing solution. Figure 2C shows data averaged from five experiments; at both 640 and 580 nm emission, a similar result was evident. At a common pH, SNARF fluorescence intensity therefore increased as the dye entered the intracellular compartment.

The nigericin–digitonin technique described above was used to estimate [SNARF]<sub>i</sub>. Figure 2D shows the results of equilibrating myocytes with two different concentrations of non-esterified SNARF (at pH<sub>o</sub> 7.17). Also shown, is the average intracellular fluorescence intensity of typical SNARF-AM-loaded myocytes selected with ratiometric pH<sub>i</sub> values close to 7.17. The fluorescence intensity of SNARF-AM-loaded cells was roughly mid-way between the nigericin–digitonin-induced fluorescence achieved with 0.276 and 0.551 mM SNARF. This indicates that intracellular [SNARF] was ~400 μM.

**Spectral changes of intracellular SNARF.** These have yet to be characterized in detail. The enhanced intracellular fluorescence indicates a considerable rise in the maximal fluorescence ( $f_{max}$ ). A small change in [SNARF] required for half-maximal fluorescence ( $f_{0.5}$ ) may also occur, as doubling [SNARF] from 0.276 to 0.551 mM increased extracellular fluorescence by 50% (Fig. 1A) but increased intracellular fluorescence by less (~30%; see Fig. 2D), despite the increase in  $f_{max}$ . An additional observation is that the enhancement of SNARF fluorescence was fractionally larger on the 640 nm signal (Fig. 2D). Consequently the ratiometric signal (640/580 nm) differed inside and outside the cell (see Fig. 2B), even when pH had been equalized by using nigericin and digitonin. This difference in the fluorescence ratio

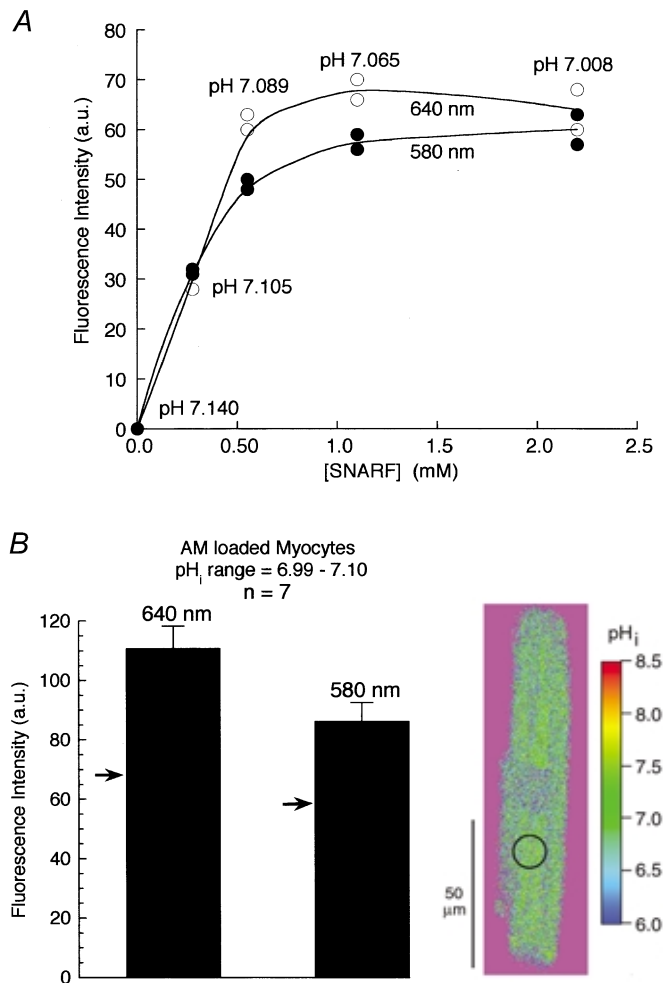


**Figure 1. Comparison of extracellular with intracellular SNARF fluorescence**

A, concentration dependence of extracellular SNARF fluorescence. Different concentrations of non-esterified SNARF were pipetted into the experimental chamber at near constant pH (at 37 °C). Excitation was at 514 nm; emission intensity, measured in arbitrary units (a.u.) at 640 and 580 nm. The range of solutions was assessed twice. B, right panel shows a pseudocoloured, calibrated ratiometric image of intracellular SNARF fluorescence in a myocyte. The colour bar refers to intracellular compartment only (i.e. extracellular solution contained no SNARF, background colour is therefore arbitrary). Circle denotes the region of interest (ROI) within which pH<sub>i</sub> was averaged. Left panel, bars show mean intracellular fluorescence intensity in an ROI (measured at 580 and 640 nm emission) in AM-loaded myocytes (intracellular pH range 6.99–7.10). Arrows indicate the fluorescence intensity from extracellular SNARF at 1.1 mM; values taken from A.

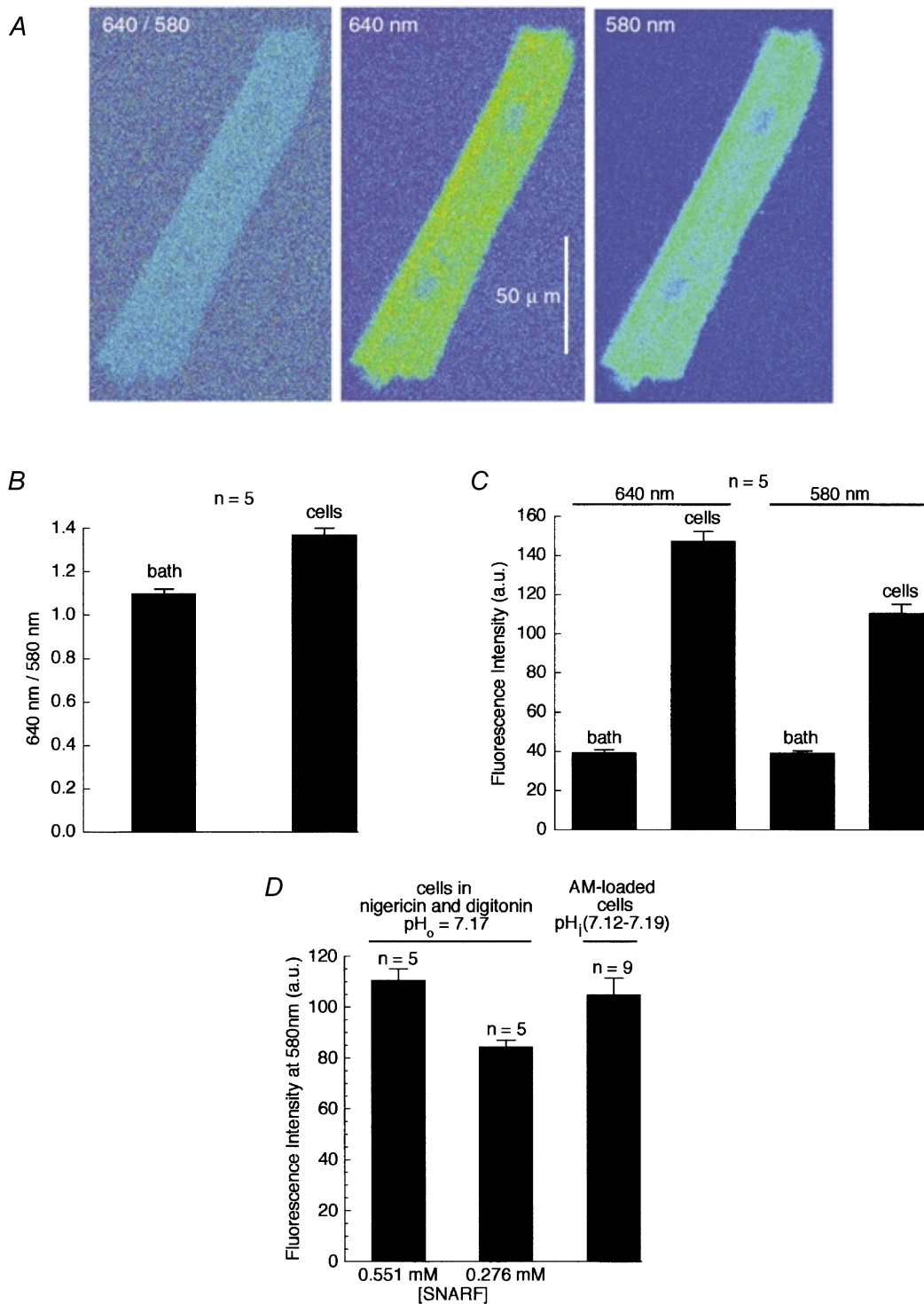


**Figure 2. Digitonin method for estimating [SNARF]<sub>i</sub>**

A, middle (640 nm emission) and right (580 nm) panels show a cell equilibrated with extracellular non-esterified SNARF (0.55 mM) plus 10  $\mu$ M digitonin, 13  $\mu$ M nigericin and 140 mM K<sup>+</sup>. Note that, despite the same intracellular and extracellular concentration of SNARF and the same pH<sub>o</sub>, 7.17, intracellular SNARF fluoresced more intensely than extracellular SNARF. Pseudocolouring from blue to yellow represents low to high fluorescence intensity in both cell and solution. Left panel shows the ratiometric SNARF signal from the same cell and solution; dark blue to light blue represents lower to higher ratiometric values. B, bars compare the ratiometric signal in cell and in solution. C, the bars show cell and bath fluorescence intensity compared at single emission wavelengths (640 and 580 nm). D, the first two bars show intracellular fluorescence intensity (at 580 nm emission wavelength) in cells loaded with 0.551 mM and 0.276 mM non-esterified SNARF. The right bar shows mean intracellular fluorescence intensity (at 580 nm) in AM SNARF-loaded cells selected to be in the same pH<sub>i</sub> range.

can be seen in the first pseudocoloured image shown in Fig. 2A. The result reinforces the generally held assumption that extracellular SNARF calibrations cannot be used to convert the intracellular ratiometric signal to a pH value; an intracellular *in situ* calibration procedure is necessary as detailed in Methods.

### Intracellular SNARF mobility

**Imaging longitudinal SNARF diffusion.** Figure 3 illustrates an experiment where non-esterified SNARF was admitted into one pole of an isolated myocyte through a cell-attached patch pipette. The pipette filling solution (see

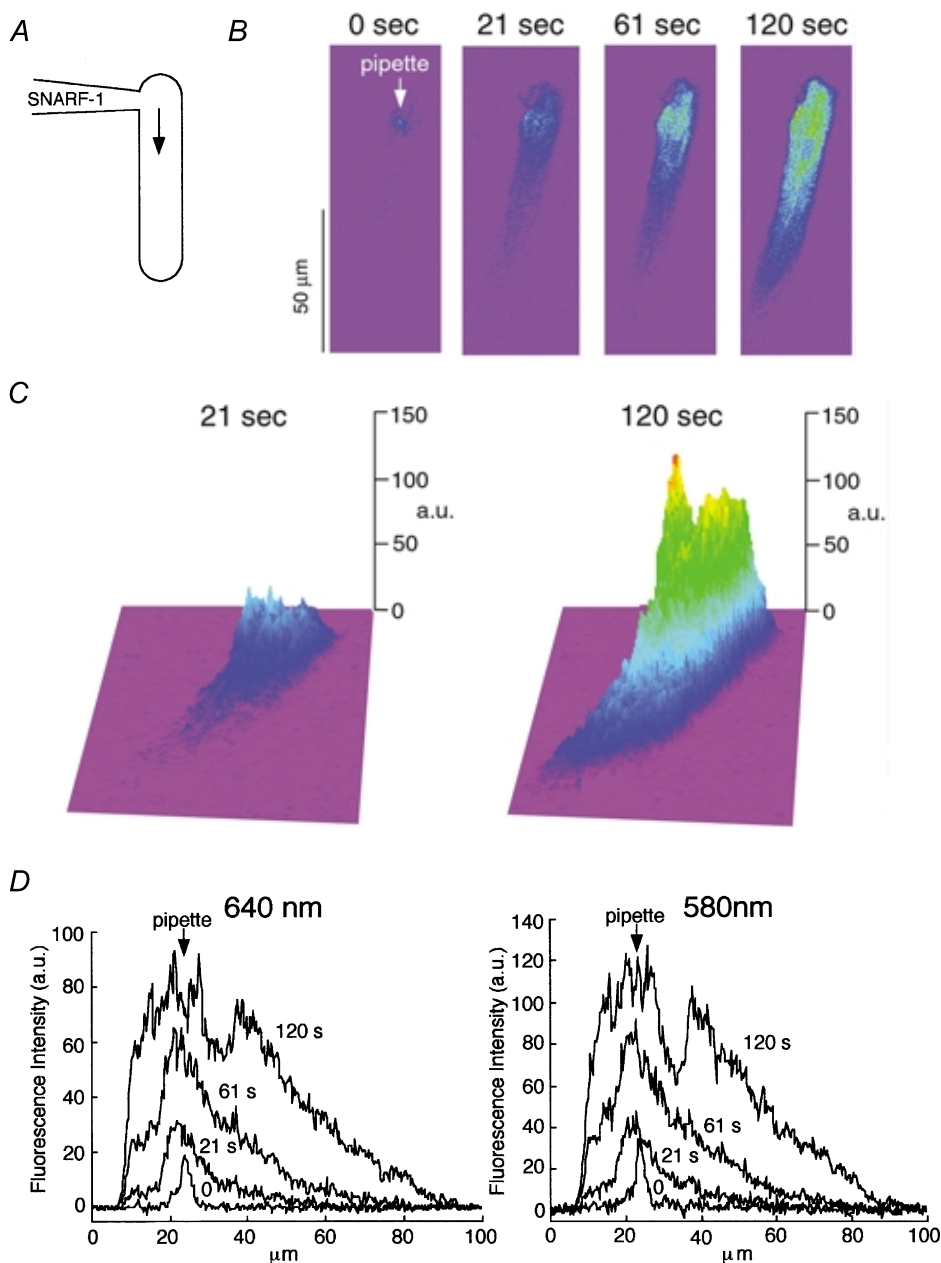


### Figure 3. Kinetics of intracellular SNARF movement

A, non-esterified SNARF (105 μM) was pipette-loaded into a myocyte. B, confocal images of SNARF fluorescence taken at various times after break-in (at 580 nm emission wavelength). Spectral pseudocolour range from violet to red represents zero to high fluorescence intensity. C, 3-D reconstructions of spatially distributed intracellular fluorescence intensity (arbitrary units, ordinate) at times indicated after pipette break-in. Note that peak fluorescence in right panel occurred at location of pipette. D, longitudinal spatial profiles of intracellular fluorescence intensity (at 640 nm, left, and at 580 nm, right) at various time intervals after pipette break-in. The myocyte extends from ~8 to ~95 μm on the abscissa. The longitudinal intensity distribution was averaged in a 5 μm wide ROI positioned down the length of the cell image. The downward notch in the peak of the two profiles at 120 s was caused by a lower signal intensity detected in the nuclear region.

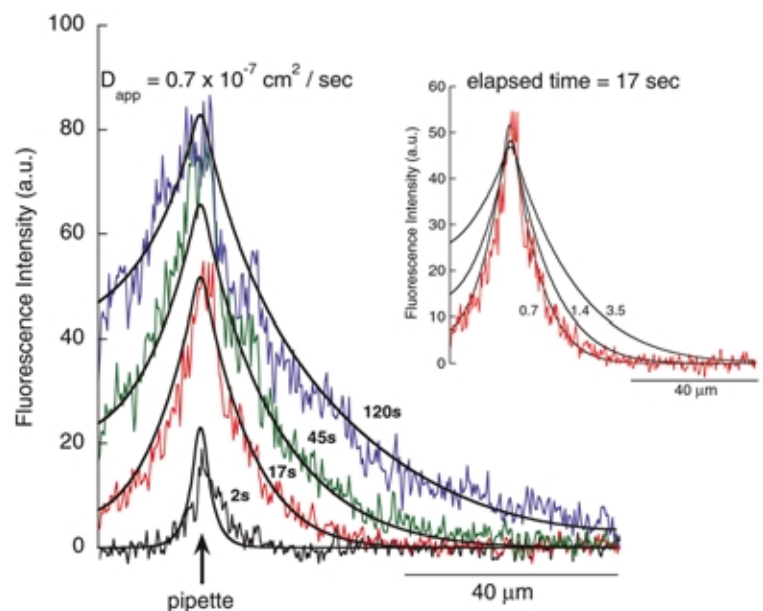
Methods) contained 105  $\mu\text{M}$  SNARF at pH 7.1, giving a pipette electrical resistance of  $\sim 1.5\ \text{M}\Omega$ . SNARF light emission from the pipette tip can be seen as a bright spot in the first of the confocal fluorescence images shown in Fig. 3B. The subsequent three panels show images obtained 21, 61 and 120 s after pipette break-in. Immediately after break-in, all pipette suction was released to equalize pipette pressure with atmospheric pressure. Figure 3C shows the spatial distribution of SNARF fluorescence intensity recorded at different times following break-in. At 21 s, SNARF intensity was greatest at the site of the pipette tip, declining monotonically with longitudinal distance from the tip. No fluorescence was detectable at the distal end. In contrast at 120 s, intensity was still greatest at the site of the tip, but fluorescence was now invading the distal end of the cell. The longitudinal spread of intracellular SNARF is quantified in Fig. 3D where measurements at increasing time intervals have been superimposed. By recording intensity at both 580 and 640 nm the diffusion rate of, respectively, the protonated and non-protonated forms of the dye can be assessed. Results at the two wavelengths were virtually identical indicating that both forms of the dye diffused at comparable rates.

#### Apparent diffusion coefficient for intracellular SNARF.

Figure 4 shows spatial profiles obtained in an experiment similar to that shown in Fig. 3. The lowest profile was obtained 2 s after pipette break-in while the highest was after 120 s. The continuous lines have been fitted to the data using the mathematical diffusion model described in Appendix. The fit to all profiles was obtained by assuming a single diffusion coefficient for SNARF<sub>i</sub> ( $0.7 \times 10^{-7}\ \text{cm}^2\ \text{s}^{-1}$ ). The sensitivity of the fitting method is illustrated in Fig. 4 inset (a SNARF profile recorded at 17 s) where different values of diffusion coefficient have been used in the fitting procedure.

#### Figure 4. Estimating intracellular SNARF diffusion coefficient

Longitudinal spatial profiles of intracellular SNARF fluorescence intensity recorded (at 640 nm) at various time-intervals after pipette break-in. Protocol same as that shown in Fig. 3, with [SNARF] in the pipette at 105  $\mu\text{M}$ . Main figure shows best-fit profiles to the data obtained with the diffusion model described in the Appendix, using a single value ( $0.7 \times 10^{-7}\ \text{cm}^2\ \text{s}^{-1}$ ) for the diffusion coefficient. The inset illustrates the sensitivity of the method, showing that 2  $\times$  and 5  $\times$  the value selected for the diffusion coefficient produced a much poorer fit.



In three pipette loading experiments with a [SNARF] of 105  $\mu\text{M}$ , the mean value for the apparent diffusion coefficient of intracellular SNARF was  $0.9 \pm 0.11 \times 10^{-7}\ \text{cm}^2\ \text{s}^{-1}$ .

#### Concentration dependence of intracellular SNARF movement.

In three experiments, the loading concentration of SNARF in the pipette was raised from 105 to 0.551  $\mu\text{M}$  and 2.2 mM, while longitudinal SNARF<sub>i</sub> movement was assessed from the delay recorded with a fixed distance between two regions of interest (ROIs, of 10  $\mu\text{m}$  diameter), one drawn at the site of the pipette and the other 40  $\mu\text{m}$  downstream. The arrival of SNARF in an ROI was defined as the moment when mean fluorescence intensity had increased to twice that of the peak-to-peak background noise. As expected, increasing the loading concentration decreased the delay for a threshold level to be detected downstream. The mean delays were, respectively,  $31 \pm 14\ \text{s}$  ( $n = 3$ ),  $24 \pm 0.74\ \text{s}$  ( $n = 2$ ) and  $11.23 \pm 3.18\ \text{s}$  ( $n = 3$ ).

#### Influence of SNARF<sub>i</sub> on intracellular acid movement

Knowing the concentration and longitudinal delay for intracellular SNARF, its contribution to intracellular acid movement can be assessed. This is considered in Discussion but it is useful to show here, by approximation, that the contribution from SNARF<sub>i</sub> will be small.

At a resting pH<sub>i</sub> of 7.1, the intracellular buffer capacity of SNARF will be about 40% of its total concentration of 400  $\mu\text{M}$ , i.e. 167  $\mu\text{M}$  ( $pK$ , 7.6), and will decline with further displacements of pH<sub>i</sub> away from its  $pK$ . Later in Results, longitudinal H<sup>+</sup> diffusion is assessed following diffusion of acid into one end of a myocyte from a cell-attached patch pipette (for example see Fig. 5). For simplicity, we can approximate the myocyte volume as three equal compartments, 33  $\mu\text{m}$  in length, joined in series. The greatest possible contribution of SNARF<sub>i</sub> to H<sup>+</sup> movement down the cell would occur if the dye were all initially

located in compartment 1 (admittedly an improbable event). SNARF could then buffer a maximum of  $167 \mu\text{mol l}^{-1}$  of injected acid and, in the extreme case, transport it to distal compartment 3. With reference to the longitudinal delays for SNARF<sub>i</sub> movement (see previous section), at  $400 \mu\text{M}$  it would take  $\sim 44$  s to travel  $66 \mu\text{m}$  from mid-compartment 1 to mid-compartment 3 (making the simplifying assumption that delay is related linearly to distance). Given that a return of the deprotonated SNARF to compartment 1 would also take at least 44 s, a maximum of  $167 \mu\text{mol l}^{-1}$  of protons would be shuttled distally by SNARF<sub>i</sub> every 88 s, an acid loading rate of  $0.11 \text{ mmol l}^{-1} \text{ min}^{-1}$ .

The acid loading rate of compartment 3 following pipette injection of acid into compartment 1 can be approximated as  $3.35 \pm 1.1 \text{ mmol l}^{-1} \text{ min}^{-1}$  ( $n = 7$ ; estimated as  $-\text{dpH}_i/\text{dt} \times \beta_i/3$ , where  $\beta_i$  is intrinsic intracellular buffering power determined at  $\text{pH}_i$  7.1 from eqn (1) in Methods, and  $\text{dpH}_i/\text{dt}$  is the rate of fall of  $\text{pH}_i$  recorded in distal ROIs in experiments such as that shown in Fig. 5). Thus the fraction of distal acid loading due to longitudinal

shuttling of acid on SNARF will be  $(0.11/3.35) \times 100 = 3.3\%$  of total distal acid loading. This is likely to be an overestimate of intracellular acid shuttling as SNARF<sub>i</sub> cannot all be located initially in compartment 1, and not all protons captured by SNARF will be discharged in the most distal compartment. Furthermore, SNARF's capacity to shuttle protons will decline as the cell acidifies. SNARF is therefore unlikely to affect significantly the present estimates of intracellular  $\text{H}^+$  ion mobility.

## Part 2. Intrinsic, intracellular $\text{H}^+$ ion mobility

### Temporal characteristics of $\text{pH}_i$ gradients

**Effect of local acid loading by pipette.** Figure 5 shows the effect on  $\text{pH}_i$  of break-in with a patch pipette containing an unbuffered filling solution consisting of  $140 \text{ mM}$  KCl, adjusted with HCl to  $\text{pH}$  3.0. Immediately following break-in, pressure in the suction pipette was equalized to atmospheric pressure. The cell had been loaded with SNARF-AM. The superfusate was nominally free of  $\text{CO}_2/\text{HCO}_3^-$  (buffered with  $24 \text{ mM}$  Hepes) and contained  $1 \text{ mM}$  amiloride to inhibit sarcolemmal acid extrusion via  $\text{Na}^+-\text{H}^+$  exchange (NHE). Figure 5A upper right panel

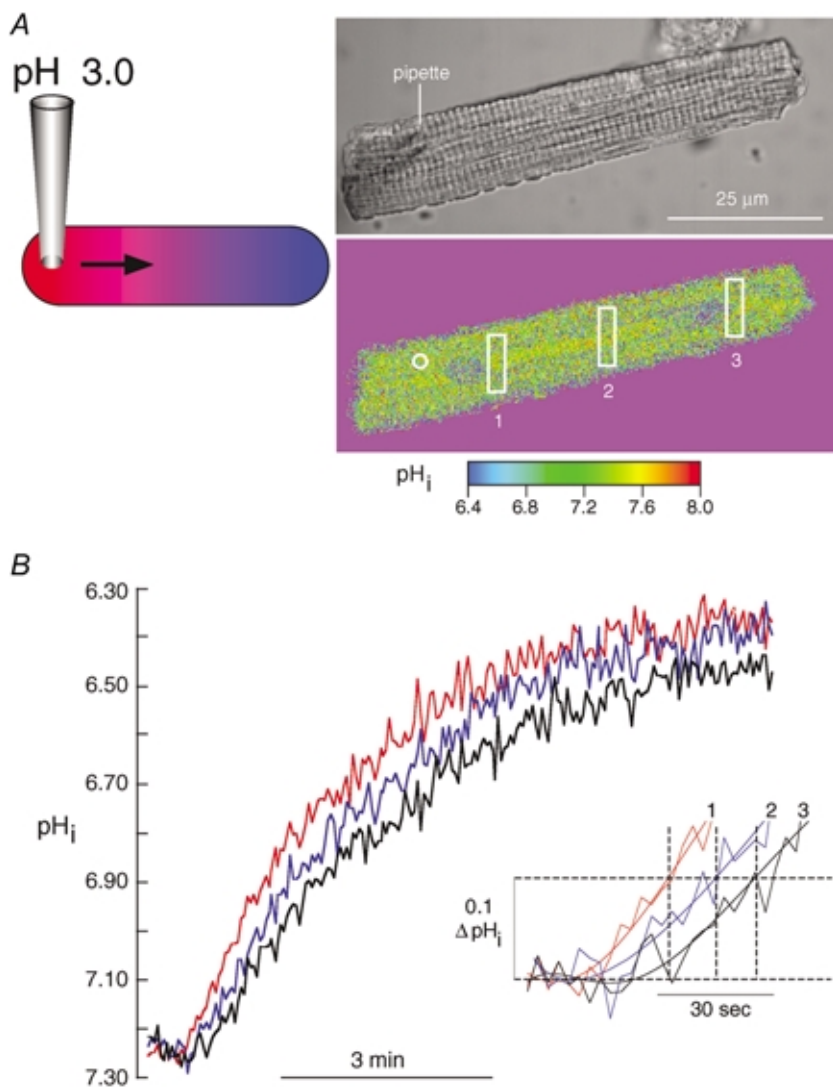


**Figure 5. Slow intracellular  $\text{H}^+$  movement**

A, break-in with a patch pipette containing isotonic KCl,  $\text{pH}$  3.0. Images show (top) position of pipette, and (bottom) ratiometric SNARF image of  $\text{pH}_i$  in same cell (note that the calibration bar refers only to the intracellular compartment; extracellular background colour is arbitrary). The circle denotes the pipette position. B, the time course of acid loading averaged for the three ROIs shown in the  $\text{pH}$  image displayed in A. ROIs were positioned to avoid nuclear regions. Inset shows early acid loading phase at higher resolution, and also shows the thresholding procedure ( $-0.1 \Delta\text{pH}_i$ ) used to estimate the moment of first arrival of  $\text{H}^+$  equivalents within an ROI. To help identify the arrival time of  $\text{pH}_i$  at the  $0.1$  threshold, polynomial fits (5th order) were applied to each curve over the first 3.9 min.

shows a transmission image of the myocyte while the lower panel shows the ratiometric confocal image of pHi. Figure 5B shows pHi averaged in three ROIs, plotted *versus* time following break-in. The ROIs are positioned downstream from the patch pipette, as indicated on the confocal image. Note that the region closest to the pipette (ROI 1) acidified at a faster rate than the more distal regions (ROIs 2 and 3).

The spread of acidification was quantified by measuring the time for pHi in proximal and distal ROIs to fall by 0.1 pH units (see inset to Fig. 5B). This 0.1 pH unit threshold was roughly twice the magnitude of peak-to-peak noise in the pHi traces and so could readily be resolved. The time taken for acid to move between ROIs 1 and 3 was 24 s. Thus the longitudinal movement of intracellular H<sup>+</sup> ions is slow. Figure 5 indicates that an acid load induced at one end of a cardiac myocyte would invade the far end of a 100 μm cell after ~70 s. Similar results were seen in six other cells.

**Effect of NHE activity.** Sarcolemmal (lateral) acid extrusion on NHE could conceivably reduce the spread of intracellular acid along a myocyte. This would be analogous to electrical cable theory where the lateral leakage of charge limits its intracellular longitudinal spread. The filled circles plotted in Fig. 6 show that omitting amiloride from the superfusate had no effect on the time delay for intracellular acid movement, indicating that lateral acid leakage does not significantly influence our estimate of intracellular H<sup>+</sup> mobility, at least not over the length of a single myocyte.

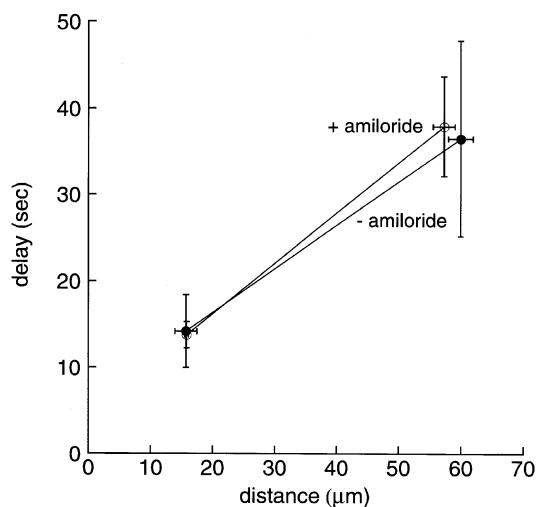


**Figure 6. Effect of amiloride on intracellular H<sup>+</sup> movement**

The time delay for arrival of intracellular H<sup>+</sup> at various ROIs has been plotted *versus* longitudinal distance from the centre of the ROI to the patch pipette. A thresholding of  $-0.1 \Delta\text{pH}_i$  was used to detect the arrival of acid. Data show results in the presence (open circles,  $n = 7$ ) and absence (filled circles,  $n = 3$ ) of 1 mM amiloride, an inhibitor of Na<sup>+</sup>-H<sup>+</sup> exchange.

### Spatial characteristics of pHi gradients

**Longitudinal pHi gradient.** In Fig. 7, the fall of pHi from its control level has been plotted as a function of longitudinal distance along the cell. The region analysed is indicated in the pHi image, and was positioned to avoid nuclear regions. The plots shown in the upper panel were obtained by subtracting a control image for the ROI, from images taken at 0, 35, 81 and 166 s after break-in. At 35 and 81 s, longitudinal pHi gradients of up to 0.4 pH units are evident. Comparable gradients were seen in six other cells (for example see Fig. 8 where, during acid loading, a pHi gradient of about 0.2 pH units is evident between ROIs 1 and 2 placed about 40 μm apart). Figure 7 shows that

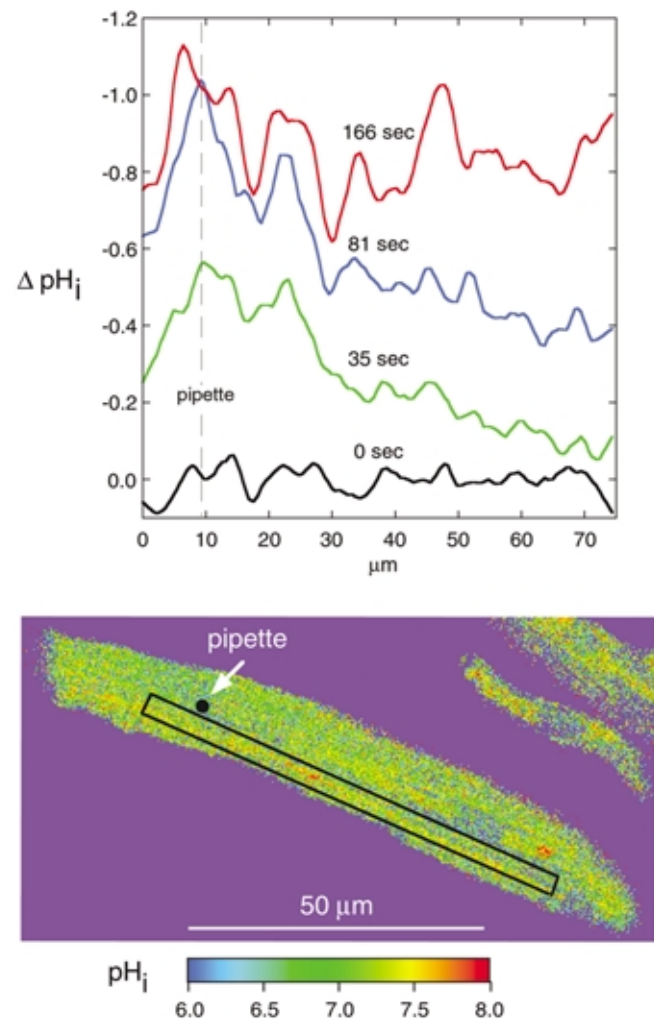


**Figure 7. Longitudinal gradients of pHi**

Lower panel shows a ratiometric pseudocoloured image of a SNARF-loaded myocyte. Note that extracellular, background coloration is arbitrary. Upper panel shows, at different time intervals following pipette break-in, the longitudinal spatial profile of pHi along the length of the rectangular ROI drawn in the lower panel. Profiles are displayed as changes of pH ( $-\Delta\text{pH}_i$ ) from the basal condition. This was achieved by subtracting the pre-existing longitudinal profile imaged at  $-5$  s from that imaged at various times following pipette break-in (defined as 0 s).

acidosis is maximal close to the pipette, and declines monotonically on either side. This longitudinal, spatial profile suggests that acidosis is not propagating as a regenerative wave down the cell, but is spreading diffusively from its source. Eventually acidosis ( $\Delta\text{pH}_i$ ) spreads to both ends of the cell resulting in a relatively uniform fall in  $\text{pH}_i$ . The large apparent undulations seen in the final longitudinal  $\Delta\text{pH}_i$  profile at 166 s are mainly comprised of signal noise as, at this  $\text{pH}_i$  (about 6.1), the SNARF dye is close to saturation by intracellular  $\text{H}^+$  ions (dye  $\text{pK} \sim 7.6$ ).

### Estimating the apparent diffusion coefficient for intracellular $\text{H}^+$

**Mathematical model of diffusion.** The diffusional model used to assess intracellular SNARF mobility was also used to estimate the apparent diffusion coefficient for intracellular  $\text{H}^+$  ions ( $D_{\text{app}}^{\text{H}}$ ). The underlying assumptions were the same, i.e. that acid equivalent movement is dictated by free (albeit apparently slow) diffusion of  $\text{H}^+$  with a unique value for the diffusion coefficient, and no intracellular buffering. Acid was assumed to enter the cell continuously from a point source located towards one (spatially defined) end of the cell. The cell was treated as a two dimensional, short cable (with end-reflection).

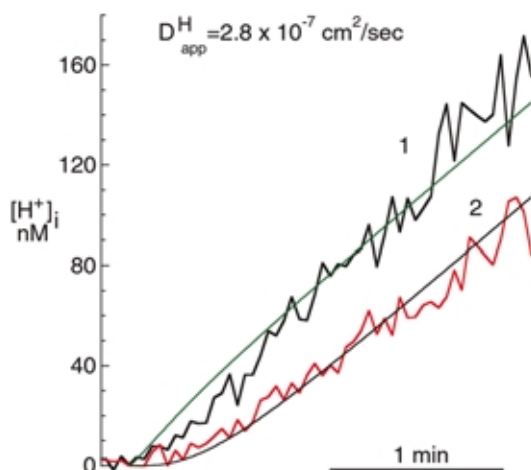
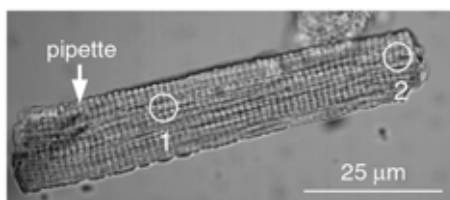


**Figure 8. Fitting the time course of rise of  $[\text{H}^+]_i$**

The time course of fall of  $\text{pH}_i$  in two defined ROIs (shown in transmission image at top) was converted to a rise in  $[\text{H}^+]_i$  from its basal level ( $\Delta[\text{H}^+]_i$ ), as shown. This was then fitted using the mathematical diffusion model described in Appendix. In the example shown, a best fit to both traces was obtained using a value for  $D_{\text{app}}^{\text{H}}$  of  $2.8 \times 10^{-7} \text{ cm}^2 \text{ s}^{-1}$ .

In the present experiments, longitudinal  $\text{pH}_i$  profiles reconstructed at different time intervals (as in Fig. 7) were resolved less well when compared with experiments on longitudinal SNARF diffusion (e.g. Figs 3 and 4), reflecting the poorer signal-to-noise ratio inherent in the ratiometric  $\text{pH}_i$  measurements. Consequently, rather than attempting to match longitudinal acid profiles, the model was used to fit the initial time course of acid loading in different ROIs down the cell, as this was more readily measured.

Figure 8 shows one example of the model-fitting procedure. In order to analyse time course, the fall in  $\text{pH}_i$  in two downstream ROIs was converted from  $\text{pH}_i$  to elevations in  $[\text{H}^+]_i$  above the control level ( $\Delta[\text{H}^+]_i$ ). The model-fitting procedure sought a single value of  $D_{\text{app}}^{\text{H}}$  that produced the best fit to both traces. In this case, the value was  $2.8 \times 10^{-7} \text{ cm}^2 \text{ s}^{-1}$ . Best fit values obtained from experiments in the absence or presence of 1 mM amiloride were not significantly different: with amiloride,  $D_{\text{app}}^{\text{H}} = 3.31 \pm 0.68 \times 10^{-7} \text{ cm}^2 \text{ s}^{-1}$  ( $n = 7$ ); without amiloride  $D_{\text{app}}^{\text{H}} = 4.87 \pm 2.82 \times 10^{-7} \text{ cm}^2 \text{ s}^{-1}$  ( $n = 3$ ). By combining both sets of data ( $n = 10$ ), an overall mean value for  $D_{\text{app}}^{\text{H}}$  of  $3.78 \pm 0.9 \times 10^{-7} \text{ cm}^2 \text{ s}^{-1}$  was obtained.

**Effect of acid loading rate.** It seemed possible that the ability to resolve a proximal–distal time delay might be dictated in the present experiments by the rate of diffusion of acid from the cell-attached patch pipette rather than by its rate of diffusion down the cell. In this case the derived value for  $D_{\text{app}}^{\text{H}}$  would not be a constant but would vary systematically with acid loading rate. We estimated this rate by measuring initial  $\text{dpH}_i/\text{dt}$  after pipette break-in, averaged for the whole area of the cell. Acid loading rate

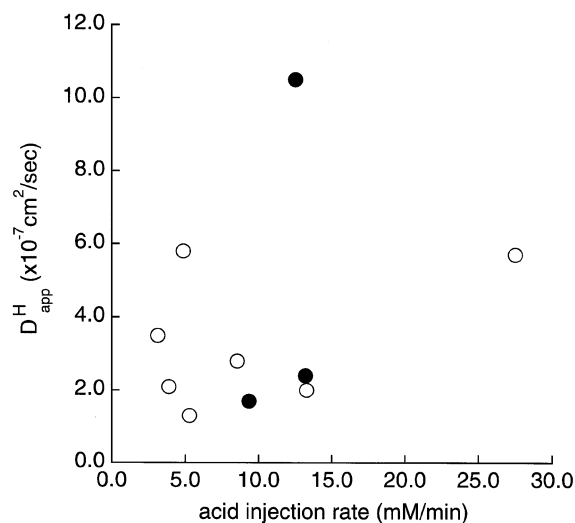


**Figure 9. Effect of acid loading rate**

Acid diffusion rate from the cell-attached pipette, estimated as whole cell  $(-\text{dpH}_i/\text{dt}) \times \beta$  (where  $\beta$  is intrinsic buffering power), is plotted versus  $D_{\text{app}}^{\text{H}}$  determined in that experiment (using the diffusional model) for experiments in the absence (open circles) or presence (filled circles) of 1 mM amiloride.

was calculated as  $dpH_i/dt \times \beta_i$ , where  $\beta_i$  was determined from the initial whole-cell pH<sub>i</sub>, using eqn (1) in Methods. The scatter plot shown in Fig. 9 indicates that there was no significant correlation between the modelled value for  $D_{app}^H$  and the acid loading rate, despite a ten-fold variation in the latter (least-squares linear regression analysis gave a correlation coefficient of 0.184). Thus the value obtained for  $D_{app}^H$  was not influenced by the rate of acid loading from the pipette.

**Quantitative relationship between intracellular diffusion delay, diffusion distance and  $D_{app}^H$**

On a diffusive model, time delay for passage of acid down a myocyte should decline as H<sup>+</sup> mobility increases. Model predictions of the time course of acid equivalent loading in proximal and distal regions are illustrated in Fig. 10A for different assumed values of  $D_{app}^H$ , using the mean cell dimensions and ROI positions obtained in our experiments (diagram at top of figure). The pipette attachment site was

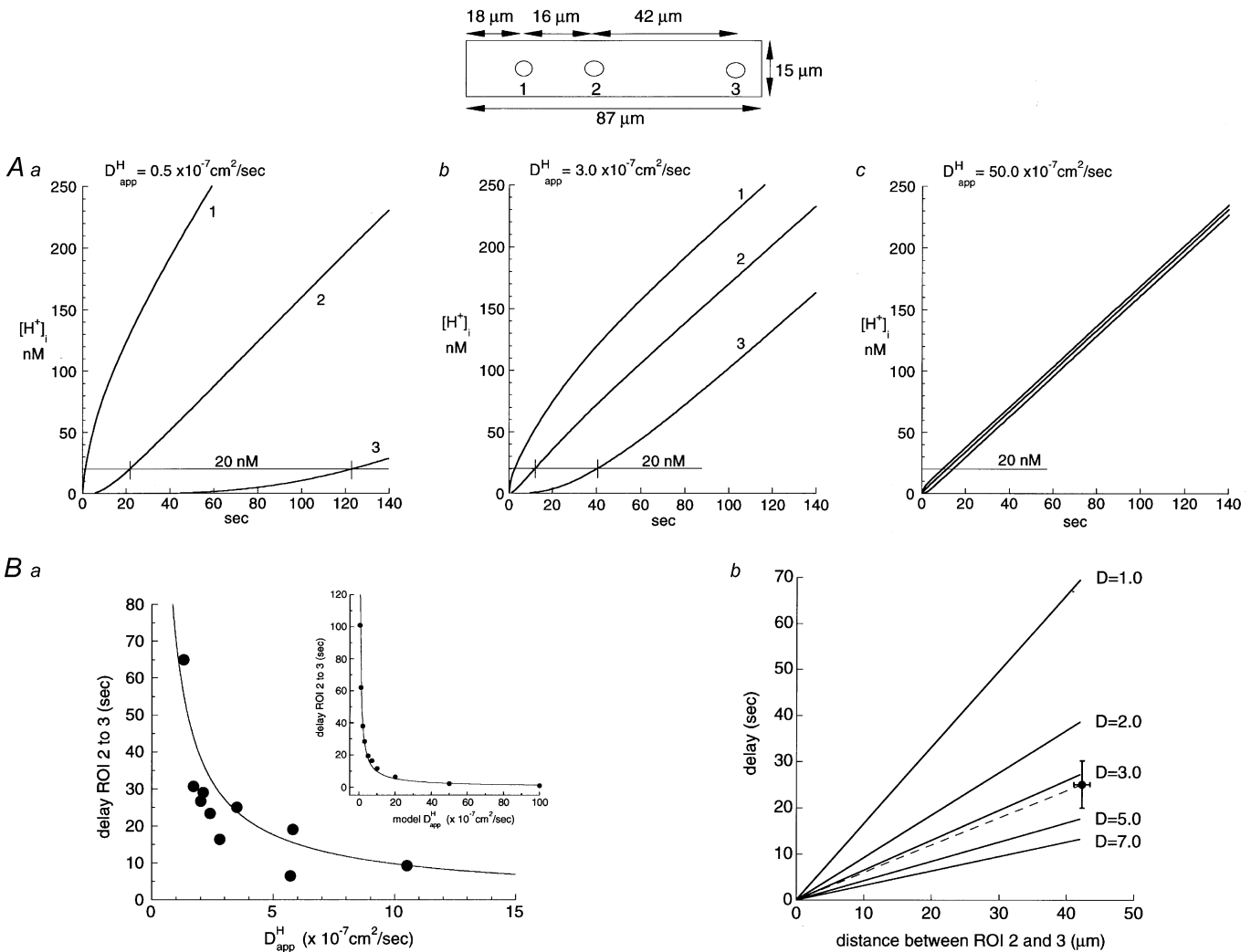


**Figure 10. Modelling H<sup>+</sup> movement**

A, time course for rise of [H<sup>+</sup>]<sub>i</sub> has been computed using the diffusion model (Appendix) for different values of  $D_{app}^H$  (a–c). Three ROIs are considered (positioned as in the top diagram, with pipette placed at ROI 1). Results are plotted in Aa–c. Results in b resemble most closely those seen experimentally. Note that as  $D_{app}^H$  rises (from a to c), the three ROIs behave more similarly, both quantitatively and temporally. B, the graph in a plots (filled circles) the experimentally measured time delay between ROI 2 and ROI 3 (see diagram at top) as a function of the value of  $D_{app}^H$  deduced by the model in that experiment. The continuous line plots the time delay predicted by the model versus assumed values of  $D_{app}^H$  (using the geometry illustrated at the top of the figure plus a 20 nM threshold rise for H<sup>+</sup>). Inset in a shows this theoretical relationship over a wider range of values for  $D_{app}^H$ . Continuous line was fitted to theoretical model predictions (filled circles) according to the equation:  $delay = 69.525(D_{app}^H)^{-0.854}$ , where the delay is expressed in seconds. b, theoretical predictions of the time delay between downstream ROIs 2 and 3 positioned 16 and 58 μm from the pipette; the delay was calculated assuming different values for  $D_{app}^H$ , as indicated. Also plotted (filled circle) is the mean delay determined experimentally ( $n = 10$ ).

at ROI 1. The three panels confirm that acid movement down a myocyte should be a function of the apparent diffusion coefficient for  $H^+$  ions ( $D_{app}^H$ ), the delay between successive time courses being less for larger values of  $D_{app}^H$ . As shown previously, the modelled time courses in Fig. 10*Ab* (for the case where  $D_{app}^H = 3 \times 10^{-7} \text{ cm}^2 \text{ s}^{-1}$ ) furnish time delays between proximal and distal ROIs that are similar to those measured experimentally (cf. Fig 8). In Fig. 10*B*, the delay between ROI 2 and ROI 3 measured in a given experiment has been plotted (filled circles) *versus* the value of  $D_{app}^H$  estimated in that experiment. The continuous line shows the delay predicted by the model at a 20 nM threshold rise of  $H^+$  over a range of  $D_{app}^H$  values (inset shows model predictions – continuous line, filled circles – for a wider range of  $D_{app}^H$  values). The line therefore provides the modelled fit to the experimental data for delay, and confirms that the higher the  $D_{app}^H$ , the lower the delay. The continuous line in Fig. 10*Ba* has been plotted according to the empirical function:

$$t = 69.525 \times (D_{app}^H)^{-0.854}, \quad (2)$$

where  $t$  equals the ROI 3–ROI 2 time delay in seconds. Provided the positioning of ROIs, the cell dimensions and the threshold value for  $\Delta[H^+]_i$  (20 nM) conform with the diagram shown at the top of Fig. 10, this empirical equation furnishes a convenient and simple way of estimating  $D_{app}^H$  from the time delay.

Predictions of the theoretical model are also illustrated in Fig. 10*Bb*. Here we have plotted the time delay predicted (at a 20 nM  $\Delta[H^+]_i$  threshold) between ROIs 2 and 3 downstream from the pipette for four different values of  $D_{app}^H$ . The mean time delay measured in our experimental work has also been plotted (filled circle) and this falls between  $D_{app}^H = 3$  and  $D_{app}^H = 5$ , consistent with the mean value of  $3.78 \times 10^{-7} \text{ cm}^2 \text{ s}^{-1}$  determined from best fitting the time courses of acid loading.

## DISCUSSION

The intrinsic mobility of intracellular acid equivalents in the ventricular myocyte ( $D_{app}^H$ ) is low, with an average value of  $3.78 \times 10^{-7} \text{ cm}^2 \text{ s}^{-1}$  at a  $pH_i$  of 7.1. This is over 300 times lower than the diffusion coefficient for  $H^+$  ions in dilute unbuffered solution ( $1187 \times 10^{-7} \text{ cm}^2 \text{ s}^{-1}$ ; Vanysek, 1999) and is  $\sim 55$ -fold lower than for free diffusion of simple inorganic ions such as  $Na^+$  or  $K^+$  ( $170$  and  $250 \times 10^{-7} \text{ cm}^2 \text{ s}^{-1}$ , respectively; Vanysek, 1999) after correcting for the  $\sim 27.5\%$  increase in  $D$  associated with increasing temperature from 2 to 3 °C (Vanysek, 1999). It is also  $\sim 4$ -fold lower than  $D_{app}^H$  estimated in extruded molluscan axoplasm at a similar  $pH_i$  (Al-Baldawi & Abercrombie, 1992) and that predicted for frog skeletal myoplasm (Irving *et al.* 1990). A lower value ( $\sim 10^{-7} \text{ cm}^2 \text{ s}^{-1}$ )

has, however, been reported recently in isolated duodenal enterocytes (Stewart *et al.* 2000).

When defining apparent intracellular  $H^+$  diffusion coefficients, we do not attempt to distinguish between the movement of  $H^+$  or the counter movement of  $OH^-$  ions, or indeed between diffusion of hydronium or hydroxonium ions. Even in simple, unbuffered solutions at physiological pH, such clear distinctions are rarely feasible. We have therefore reported values for the apparent mobility of intracellular  $H^+$  or its ionic equivalent. We show below, however, that effective intracellular  $H^+$  mobility depends not upon free diffusion of  $H^+$  or  $OH^-$  ions but upon diffusion of  $H^+$  equivalents conjugated to intracellular buffers. In the context of a cell's physiology, the question of whether an intracellular acid flux is dictated by the unbuffered movement of  $H^+$  or  $OH^-$  or their hydrated forms becomes less important, to be replaced by an analysis of intracellular buffer concentration, buffer pK and buffer mobility.

### Suitability of SNARF for $pH_i$ imaging

**SNARF contribution to intracellular acid equivalent mobility.** Our measurements of intracellular SNARF concentration (0.4 mM), when combined with our estimates of intracellular SNARF mobility ( $0.9 \times 10^{-7} \text{ cm}^2 \text{ s}^{-1}$ ) indicate that very little intracellular acid movement is caused by the shuttling of  $H^+$  ions on SNARF itself. In Results, we approximated this fraction to be  $< 3.3\%$ . Thus most acid moves via some other route. The most likely route is a shuttling of acid on intrinsic, intracellular buffers, as proposed by Junge & McLaughlin (1987). We consider this in more detail later in Discussion. Suffice it to say here that, on such a model, the amount of acid carried by SNARF will be apportioned according to the concentration, pK and mobility of SNARF relative to that of the cellular intrinsic buffers. Intrinsic  $H^+$  buffering power ( $\beta_i$ ) is about 27 mM at  $pH_i$  7.10 (Leem *et al.* 1999) whereas that for SNARF is  $\sim 0.17$  mM (see Results). Provided intracellular mobile buffer is not saturated, the apparent diffusion coefficient averaged for all intracellular buffers, including SNARF ( $D_{app}^B$ ) can be described as (Junge & McLaughlin, 1987; Irving *et al.* 1990):

$$D_{app}^B = (\beta_i D_{intrinsic})/\beta_{tot} + (\beta_{SNARF} D_{SNARF})/\beta_{tot}, \quad (3)$$

where  $D_{intrinsic}$  is the mean diffusion coefficient for all intrinsic, intracellular buffers combined,  $D_{SNARF}$  is the diffusion coefficient for intracellular SNARF ( $0.9 \times 10^{-7} \text{ cm}^2 \text{ s}^{-1}$ ),  $\beta_{SNARF}$  is the buffering capacity for intracellular SNARF ( $0.17 \text{ mmol l}^{-1} \text{ min}^{-1}$ ) at a concentration of 0.4 mM and a  $pH_i$  of 7.10 (SNARF pK  $\sim 7.60$ ), and  $\beta_{tot}$  is the total intracellular buffering power (where  $\beta_{tot} = \beta_i + \beta_{SNARF}$ ). As discussed below, the buffer model of  $H^+$  mobility predicts that, in the absence of

SNARF,  $D_{\text{app}}^{\text{H}} \approx D_{\text{app}}^{\text{B}} = D_{\text{intrinsic}}$  (i.e. when  $\beta_i = \beta_{\text{tot}}$ , the first term in eqn (3) becomes  $D_{\text{intrinsic}} = D_{\text{app}}^{\text{B}} = 3.8 \times 10^{-7} \text{ cm}^2 \text{ s}^{-1}$ ). Adding the second term of eqn (3) will indicate the effect on overall buffer mobility (and hence on acid equivalent mobility) of adding SNARF to the intracellular compartment. Substituting the values listed above increases the value of  $D_{\text{app}}^{\text{B}}$  by  $\sim 0.6\%$ , i.e.  $D_{\text{app}}^{\text{B}}$  remains close to  $3.8 \times 10^{-7} \text{ cm}^2 \text{ s}^{-1}$ .

We conclude that the effect of SNARF<sub>i</sub> on acid movement mediated through a buffer shuttle can be ignored, as the fluorophore's buffering power and intracellular mobility make an insignificant contribution to the total flux of buffer within the cell.

**Spectral shifts for SNARF when intracellular.** We find that there is a significant change in SNARF fluorescence as it enters the ventricular myocyte. At a given pH, the fluorescence maximum ( $f_{\text{max}}$ , seen at high concentrations of the dye) increases and there is probably a small shift in  $f_{0.5}$  in the direction of lower SNARF concentrations. The cause of these changes is not known but they are not unique to SNARF. Intracellular spectral shifts have been observed for most other ion fluorophores (for example see Konishi *et al.* 1988; Donoso *et al.* 1992). Indeed evidence of a significant intracellular shift in  $f_{\text{max}}$  for SNARF was apparent in previous work (Bassnett *et al.* 1990; Blank *et al.* 1992). We report here that the spectral changes in SNARF lead to a change in the dye ratio for a given pH. This reinforces the widely held view that extracellular pH calibrations of dye ratio are not appropriate for quantifying the intracellular ratiometric signal. An *in situ* calibration procedure is required (see Methods).

**Estimating intracellular SNARF concentration.** Spectral shifts for intracellular SNARF meant that we developed a novel *in situ*, nigericin–digitonin method for estimating AM-loaded [SNARF]<sub>i</sub> (see Results) This method may now prove useful for estimating [SNARF]<sub>i</sub> in other cell types. It is notable that, apart from the present work, there is no study that has quantified the intracellular concentration of AM-loaded SNARF using intracellular SNARF calibration techniques. Given that intracellular SNARF concentration may vary greatly among cell types, and that this may influence basal H<sup>+</sup> ion mobility, the adoption of an internal calibration method is essential.

**Comparison with previous estimates of fluorophore mobility.** When using a two-dimensional mathematical model of diffusion, a single value of  $D_{\text{SNARF}}$  was sufficient to account reasonably well for the spatial profiles of SNARF fluorescence intensity within the cardiomyocyte. It was therefore considered unnecessary to pursue three-dimensional spatial modelling of SNARF. Our mean value for  $D_{\text{SNARF}}$  ( $0.9 \times 10^{-7} \text{ cm}^2 \text{ s}^{-1}$ ) is close to that determined for Indo-1 in rat cardiomyocytes (Blatter & Wier, 1990;

$D_{\text{Indo}} = 1.6 \times 10^{-7} \text{ cm}^2 \text{ s}^{-1}$ ) but  $\sim 3$ -fold lower than that estimated by the same authors for fura-2. No previous intracellular estimates of  $D_{\text{SNARF}}$  are available for any eukaryotic cell.

### Confocal imaging of intracellular pH in the ventricular myocyte

**Resting non-uniformities of pH<sub>i</sub>.** Diffusion of acid from a cell-attached pipette induces large gradients of pH<sub>i</sub> under non steady-state conditions (Fig. 7). Measurements of H<sup>+</sup> mobility based on these experiments suggest that non-uniformity should collapse within a few minutes of removal of the source of acid. While pH<sub>i</sub> uniformity was observed in many cells at rest, others displayed a significant degree of spatial heterogeneity (for example see Figs 1B and 5). Typically, pH<sub>i</sub> in nuclear regions (usually believed to be diffusively coupled to the cytoplasm) appeared more acidic (Fig. 5). Furthermore, a longitudinal columnar arrangement of the fluorescence ratio was sometimes evident within a cell, particularly in multinucleated myocytes where fluorescent bands were discerned spanning the space between nuclei (Figs 1B and 5). It is notable, however, that in cells exposed to nigericin, the intracellular ratiometric signal consistently became more uniform (e.g. the left panel in Fig. 2A), suggesting that much of the non-uniformity reflected a true variation in pH.

Probably the simplest explanation for spatial pH<sub>i</sub> heterogeneity at rest is the inclusion of SNARF in subcellular as well as cytoplasmic compartments. Although more than 95% of the dye is located in the cytoplasm (Blank *et al.* 1992; Spitzer & Bridge, 1992) if a sufficient amount were to enter, say, mitochondria (which possess an alkaline interior) then a non-cytoplasmic ratiometric signal with a different pH may also become detectable. Although such a small subcellular space is unlikely to be resolved accurately with SNARF fluorescence, mitochondrial signals have been reported (Chacon *et al.* 1994) and may account for some of the longitudinal banding.

In the present work we selected standard sized regions of interest (ROIs) (but avoiding nuclear regions) for analysis in our acid loading experiments. Any pH heterogeneity was thus averaged within an ROI. If organellar signals were co-expressed with cytoplasmic signals within these areas, then an error in the estimate of cytoplasmic pH<sub>i</sub> may have occurred. This, however, was deemed to be preferable to the selective avoidance of particular intracellular areas where we had no compelling evidence that such areas were not cytoplasmic in origin.

**Intracellular H<sup>+</sup> ion mobility.** Acid introduced into one end of a myocyte spreads slowly, with  $\sim 70$  s elapsing before invading the distal end. The simplest explanation for acid movement is that it is limited by the diffusion of

intracellular buffers. As these are of high capacity ( $\sim 27$  mM or more, depending on  $\text{pH}_i$ ; Leem *et al.* 1999) they will buffer almost all injected acid. Provided some of the intracellular buffers are mobile (see below), the longitudinal flux of acid will be dominated by movement of  $\text{H}^+$  ions reversibly bound to buffer. At physiological values of  $\text{pH}_i$ ,  $[\text{H}^+]_i$  is sufficiently low ( $\sim 80$  nM) that, by comparison with the size of the buffer flux, the free flux of  $\text{H}^+$  ions will be insignificant. The shuttling of  $\text{H}^+$  by intracellular buffer is illustrated diagrammatically in the top panel of Fig. 11. The buffers capture  $\text{H}^+$  ions proximal to the pipette and discharge them in more alkaline distal regions, the unloaded buffer then returning to the proximal region to repeat the cycle.

An important consequence of buffer-mediated  $\text{H}^+$  movement is that, although the rate of free  $\text{H}^+$  movement is slow ( $\sim 1\text{--}2 \mu\text{m s}^{-1}$ ), total longitudinal flux of acid (free  $\text{H}^+$  plus buffered  $\text{H}^+$ ) can be large, given the high capacity of mobile buffer. These buffers can therefore supply  $\text{H}^+$  ions to sarcolemmal membrane transporters such as  $\text{Na}^+\text{--H}^+$  exchange at a fast rate while minimizing local changes in cytoplasmic pH.

Much intracellular, intrinsic (non- $\text{CO}_2$ ) buffering comprises histidine and other  $\text{H}^+$  titratable groups on intracellular proteins. Proteins are typically polyvalent and of high molecular weight and therefore have low cytoplasmic mobility, being effectively anchored within the cell. Acid may be shuttled longitudinally through these buffers by  $\text{H}^+$  ions hopping along tracks of adjacent  $\text{H}^+$  titratable sites, as illustrated in the bottom panel of Fig. 11. In contrast, smaller non-protein buffers will have a higher mobility so that, in addition to ion hopping between adjacent buffer sites (on the same or between adjacent buffers),  $\text{H}^+$  movement will be enhanced by simultaneous diffusion of the  $\text{H}^+$  binding sites themselves. Movement of  $\text{H}^+$  in a mixed buffer population such as that found inside the cell may be a mixture of the two extremes shown in Fig. 11.

Theoretical models of ion shuttling by intracellular buffer diffusion have been developed for intracellular  $\text{H}^+$  (Junge & McLaughlin, 1987; Irving *et al.* 1990), as well as for intracellular  $\text{Ca}^{2+}$  (e.g. Zhou & Neher, 1993). Provided the buffers are not saturated by  $\text{H}^+$  ions, the apparent  $\text{H}^+$  diffusion coefficient,  $D_{\text{app}}^{\text{H}}$ , can be approximated as the sum of the diffusion coefficients for all intracellular buffers weighted according to their individual buffering power and mobility:

$$D_{\text{app}}^{\text{H}} = (2.3[\text{H}^+]D_{\text{H}})/\beta_{\text{tot}} + \sum\{(\beta_i D_i)/\beta_{\text{tot}}\}, \quad (4)$$

where the second term on the right hand side represents the summed contribution to  $D_{\text{app}}^{\text{H}}$  from the various mobile buffers within the cell, each with its own intrinsic diffusion coefficient ( $D_i$ ) while the first term represents the contribution from  $\text{H}^+$  ion diffusion in the presence of immobile buffer (e.g. buffer sites on intracellular proteins). In the absence of mobile buffer  $D_{\text{app}}^{\text{H}}$  can therefore be approximated from the first term only in eqn (4). Assuming a value for the  $\text{H}^+$  diffusion coefficient in unbuffered solution ( $D_{\text{H}} \sim 10^{-4} \text{ cm}^2 \text{ s}^{-1}$ ) the predicted value for  $D_{\text{app}}^{\text{H}}$  in the absence of mobile buffer becomes very small:  $6.5 \times 10^{-10} \text{ cm}^2 \text{ s}^{-1}$ , i.e. 150000-fold lower than  $D_{\text{H}}$ , and 600-fold lower than intrinsic  $D_{\text{app}}^{\text{H}}$  determined experimentally in the cardiomyocyte. Indeed, in the range down to  $\text{pH}_i$  4.0, the first term in eqn (4) is sufficiently small that it may be ignored. Given the extremely low predicted  $\text{H}^+$  mobility in the absence of mobile buffer, the somewhat faster mobility of  $\text{H}^+$  measured experimentally suggests that it is principally dependent on a mobile buffer shuttle (Fig. 11, top panel) rather than on the rate of fixed-site  $\text{H}^+$  ion hopping (Fig. 11, bottom panel).

A literature search (summarized in Table 1) reveals many potential sources of intracellular intrinsic mobile buffer. These include intracellular taurine,  $\text{P}_i$ , plus several derivatives of the histidine-based dipeptides carnosine, anserine and homocarnosine. Miller and colleagues (O'Dowd *et al.* 1988; House *et al.* 1989) have highlighted several of these. At a  $\text{pH}_i$  of 7.10, the total buffer capacity of

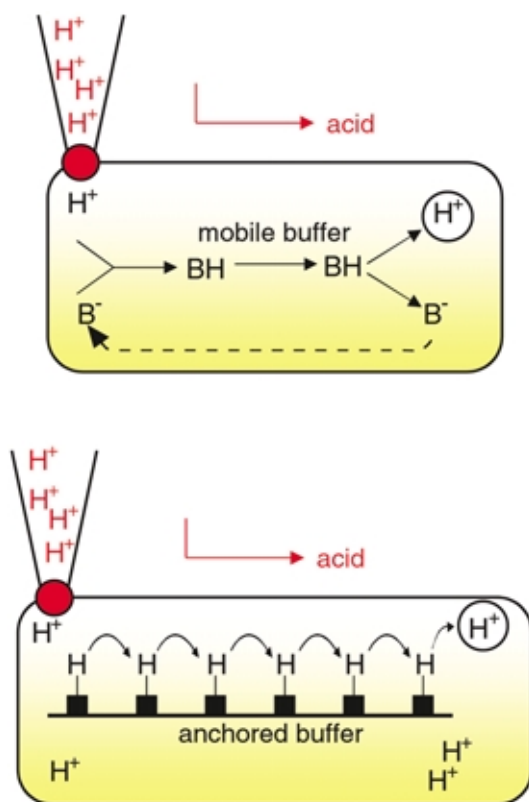


**Figure 11. Models of intrinsic  $\text{H}^+$  mobility**

Top, mobile buffer shuttling of  $\text{H}^+$ . Bottom, fixed (anchored) buffer hopping of  $\text{H}^+$ .

**Table 1. Intracellular mobile buffering power**

Mobile buffer	Concentration (mM)	pK <sub>1</sub>	pK <sub>2</sub>	pK <sub>3</sub>	β (mM/pH)
Alanine	2.80 <sup>a</sup>	2.33 <sup>α</sup>	9.71	—	0.016
Arginine	0.33 <sup>b</sup>	2.03 <sup>α</sup>	9.00	12.10	0.009
Aspartate	1.60 <sup>c</sup>	1.95 <sup>α</sup>	3.71	9.66	0.011
Glutamate	4.70 <sup>d</sup>	2.16 <sup>α</sup>	4.15	9.58	0.046
Histidine	0.56 <sup>e</sup>	1.70 <sup>α</sup>	6.04	9.09	0.109
Lysine	0.80 <sup>f</sup>	2.15 <sup>α</sup>	9.16	10.67	0.016
Taurine	29.50 <sup>g</sup>	1.50 <sup>β</sup>	9.06	—	0.666
Valine	0.31 <sup>h</sup>	2.27 <sup>α</sup>	9.52	—	0.003
Carnitine	1.50 <sup>i</sup>	3.80 <sup>β</sup>	—	—	0.002
Carnosine	0.24 <sup>j</sup>	2.51 <sup>α</sup>	6.76	9.35	0.126
Homocarnosine	9.50 <sup>k</sup>	6.92 <sup>γ</sup>	10.10	—	5.263
N-acetylhistidine	0.73 <sup>l</sup>	2.88 <sup>γ</sup>	7.01	—	0.416
N-acetyl methylhistidine	0.36 <sup>m</sup>	2.88 <sup>δ</sup>	7.01	—	0.205
N-acetylcarnosine	2.10 <sup>n</sup>	3.51 <sup>ε</sup>	7.76	10.35	0.716
N-acetylsarserine	4.00 <sup>o</sup>	3.64 <sup>ζ</sup>	8.04	10.49	0.858
ATP (Mg)	7.50 <sup>p</sup>	5.10 <sup>η</sup>	—	—	0.169
P <sub>i</sub>	4.60 <sup>q</sup>	6.90 <sup>θ</sup>	—	—	2.513
PCr	25.0 <sup>r</sup>	4.60 <sup>η</sup>	—	—	0.181
Citrate	0.36 <sup>s</sup>	3.13 <sup>β</sup>	4.76	6.40	0.119
Lactate	1.50 <sup>t</sup>	3.86 <sup>β</sup>	—	—	0.002
Total = 11.4 mM					

The concentration values (mM) are given as mmol (l intracellular H<sub>2</sub>O)<sup>-1</sup>. The buffer values (β) were calculated for pH<sub>i</sub> = 7.1 from the concentrations (mM) and pK values using a modification of the buffer equation from Leem *et al.* (1999):

$$\beta = \frac{2.303 [\text{mM}] \times 10^{(\text{pH}_i - \text{pK}_1)}}{[1 + 10^{(\text{pH}_i - \text{pK}_1)}]^2} + \frac{2.303 [\text{mM}] \times 10^{(\text{pH}_i - \text{pK}_2)}}{[1 + 10^{(\text{pH}_i - \text{pK}_2)}]^2} + \frac{2.303 [\text{mM}] \times 10^{(\text{pH}_i - \text{pK}_3)}}{[1 + 10^{(\text{pH}_i - \text{pK}_3)}]^2}$$

<sup>a, i, q, s, t</sup> Concentrations taken from Randall & Tubbs (1979). Whole-tissue concentrations expressed as μmol (g dry wt)<sup>-1</sup> were converted to mmol (l intracellular H<sub>2</sub>O)<sup>-1</sup> using the non-mitochondrial intracellular water data from the same reference (i.e. 1.85 ml H<sub>2</sub>O (g dry wt)<sup>-1</sup>).

<sup>b, e, f, h</sup> Concentrations taken from Peterson *et al.* (1973). Whole-tissue concentrations expressed as μmol (g dry wt)<sup>-1</sup> were converted to mmol (l intracellular H<sub>2</sub>O)<sup>-1</sup> using 1.85 ml H<sub>2</sub>O (g dry wt)<sup>-1</sup>.

<sup>c, d</sup> Concentrations taken from Suleiman & Chapman (1993). Whole-tissue concentrations expressed as mmol (kg wet wt)<sup>-1</sup> were converted to mmol (l intracellular H<sub>2</sub>O)<sup>-1</sup> taking intracellular water to be 64 % of the wet weight and myoplasm as 90 % of the intracellular water (Jacobus *et al.* 1982).

<sup>g</sup> Concentration taken from Takihara *et al.* (1986) and converted from μmol (g wet wt)<sup>-1</sup> to mmol (l intracellular H<sub>2</sub>O)<sup>-1</sup> using the intracellular water determinations of Jacobus *et al.* (1982).

<sup>j, l, m, n, o</sup> Concentrations taken from O'Dowd *et al.* (1988) and converted from mmol (kg wet wt)<sup>-1</sup> to mmol (l intracellular H<sub>2</sub>O)<sup>-1</sup> using the intracellular water determinations of Jacobus *et al.* (1982).

<sup>k</sup> Concentration taken from House *et al.* (1989) and converted from mmol (kg wet wt)<sup>-1</sup> to mmol (l intracellular H<sub>2</sub>O)<sup>-1</sup> using the intracellular water determinations of Jacobus *et al.* (1982).

<sup>p</sup> Concentration taken from Allen *et al.* (1985) and converted from μmol (g wet wt)<sup>-1</sup> to mmol (l intracellular H<sub>2</sub>O)<sup>-1</sup> using the intracellular water determinations of Jacobus *et al.* (1982).

<sup>r</sup> Concentration (mmol (l intracellular H<sub>2</sub>O)<sup>-1</sup>) taken from Allen & Orchard (1987).

<sup>α</sup> pK<sub>a</sub> values from Lide (2001a).

<sup>β</sup> pK<sub>a</sub> values from Lide (2001b).

<sup>γ</sup> pK<sub>a</sub> values from D. J. Miller (personal communication).

<sup>δ</sup> pK assumed to be equal to N-acetylhistidine.

<sup>ε</sup> Acetylation assumed to increase pK values by 1 unit above those for carnosine.

<sup>ζ</sup> Acetylation assumed to increase pK values by 1 unit above that for anserine (i.e. pK<sub>1</sub> = 2.64; pK<sub>2</sub> = 7.04; pK<sub>3</sub> = 9.49 from Windholz (1976)).

<sup>η</sup> pK from Gadian *et al.* (1982).

<sup>θ</sup> pK from Jacobus *et al.* (1982).

the possible non-protein intracellular buffers equals 11.4 mM (see Table 1). At the same pH<sub>i</sub>, the total intrinsic buffering power, β<sub>tot</sub>, estimated from eqn (1) (Methods) is 26.8 mM. Given the relatively low molecular weight of

the buffers listed in Table 1, their pK values close to physiological pH, and their relatively high combined concentration, it is entirely feasible that mobile buffer shuttling accounts for intracellular proton movement in

the heart. In this case, provided buffers are not saturated, the diffusion coefficient for all the mobile buffers combined ( $D_{\text{mob}}$ ; Table 1) can be approximated by re-arranging the equation (Junge & McLaughlin, 1985; Irving *et al.* 1990):

$$D_{\text{app}}^{\text{H}} = D_{\text{mob}}(\beta_{\text{mob}}/\beta_{\text{tot}}), \quad (5)$$

where  $\beta_{\text{mob}}$  equals the mean buffer capacity for intracellular mobile buffers (11.4 mM). Based on the experimentally determined value for  $D_{\text{app}}^{\text{H}}$  ( $3.78 \times 10^{-7} \text{ cm}^2 \text{ s}^{-1}$ ) and  $\beta_{\text{tot}}$  (26.8 mM), we estimate  $D_{\text{mob}}$  would be  $8.9 \times 10^{-7} \text{ cm}^2 \text{ s}^{-1}$ .

The lower value of  $D_{\text{app}}^{\text{H}}$  in myocardial cells ( $3.78 \times 10^{-7} \text{ cm}^2 \text{ s}^{-1}$ ) compared with that for extruded *Myxicola* axoplasm ( $1.4 \times 10^{-6} \text{ cm}^2 \text{ s}^{-1}$ ; Al-Baldawi & Abercrombie, 1992) may reflect a lack of physical restriction to buffer diffusion in the latter, as well as to differences in buffer type between mammalian and molluscan cells. The diffusive path of an  $\text{H}^+$  ion buffer will be more tortuous, and therefore slower in an intact myocyte than in extruded cytoplasm, because of invaginating t-system and SR membranes, and the myofilaments.  $D_{\text{app}}^{\text{H}}$  quoted for frog skeletal myoplasm ( $1$  to  $2 \times 10^{-6} \text{ cm}^2 \text{ s}^{-1}$ ; Irving *et al.* 1990) is also higher than for cardiac  $D_{\text{app}}^{\text{H}}$ , although it should be stressed that the former value was not measured experimentally, but was predicted from mobilities assumed for the intracellular buffers. The lower mitochondrial density in white skeletal muscle compared with heart may, however, mean that physical restrictions to buffer movement are less, resulting in a higher value for  $D_{\text{app}}^{\text{H}}$ .

Finally, while we have described intrinsic  $\text{H}^+$  ion mobility in terms of buffer movement, we do not exclude the possibility that some  $\text{H}^+$  equivalent flux may be tempered by rapid sequestration of  $\text{H}^+$  into organelles such as the sarcoplasmic reticulum or mitochondria. Such sequestration sites would be analogous to the anchored  $\text{H}^+$  hopping sites shown in Fig. 11 (bottom panel).

### Mathematical model of intracellular $\text{H}^+$ ion mobility

The model used to estimate  $D_{\text{app}}^{\text{H}}$  (see Appendix) describes acid equivalent mobility in terms of simple  $\text{H}^+$  ion diffusion, with no reference to the true mechanism of  $\text{H}^+$  movement (for example, with no reference to intracellular diffusible buffers). Indeed if the value for intracellular buffering power were to change significantly during an acid load, then the model would fail to predict the time course of acid loading correctly. Total intrinsic buffering power does indeed increase upon a decrease in  $\text{pH}_i$  (Leem *et al.* 1999), while the combined buffering capacity of the mobile buffers listed in Table 1 decreases at  $\text{pH}_i < 6.70$  (which, from eqn (5) would decrease  $D_{\text{app}}^{\text{H}}$ ), implying that the model may satisfactorily reproduce acid loading for small but not large displacements of  $\text{pH}_i$ . For this reason we have not attempted to model later phases of the intracellular acid loading curve.

### Plateau $\text{pH}_i$

Intracellular acid loading typically reached a steady state close to  $\text{pH}_i$  6.0 (e.g. Fig. 5B) despite the fact that the pipette filling solution was usually at  $\text{pH}$  3.0. The reason for this is not known but, in the absence of amiloride in the superfusate, a likely cause would be acid extrusion via NHE as this can be as high as  $12 \text{ mmol l}^{-1} \text{ min}^{-1}$  at  $\text{pH}_i$  6.5 (Leem *et al.* 1999). In other experiments (e.g. Fig. 5B), however, when 1–2 mM extracellular amiloride was present to inhibit NHE,  $\text{pH}_i$  still typically reached a plateau at  $\text{pH}_i$  6.0 (note that intracellular SNARF calibrates down to  $\text{pH}$  5.5). Other explanations for the plateau must therefore be sought. The possibility at low  $\text{pH}_i$  of major acid extrusion on reverse-mode sarcolemmal  $\text{Cl}^-$ – $\text{OH}^-$  exchange is unlikely as low  $\text{pH}_i$  inactivates CHE activity (Leem *et al.* 1999). One possibility is that not all acid diffusing from the pipette enters the cell, some may leak out across the membrane–electrode seal. Leakage need not be electrogenic if accompanied by outward leakage of  $\text{Cl}^-$  or a counter inward leakage of  $\text{Na}^+$  ions. Another possibility is that cytoplasm diffusing into the pipette tip tempers the  $\text{H}^+$  ion gradient that drives acid diffusion into the cell. Complex gradients at the tip have been modelled for dye injection experiments (Imanaga *et al.* 1987).

In some cells, a degree of  $\text{pH}_i$  non-uniformity remained in the plateau region (with distal regions  $\sim 0.1$   $\text{pH}_i$  units more alkaline; e.g. Fig. 5B). One explanation is that, at low  $\text{pH}_i$ , several intracellular mobile buffers are close to saturation (for example, many of the mobile buffers listed in Table 1 have  $\text{pK}$  values between 6.8 and 7.1), with the consequence that  $D_{\text{app}}^{\text{H}}$  will decline, resulting in the persistence of longitudinal  $\text{pH}_i$  gradients. Indeed a decline in  $D_{\text{app}}^{\text{H}}$  at low  $\text{pH}$  has been reported for extruded *Myxicola* axoplasm (Al-Baldawi & Abercrombie, 1992). Alternatively, intracellular mobile buffers may be dialysed out of the cell after several minutes following pipette break-in, again reducing apparent  $\text{H}^+$  mobility. Such dialysis, however, is unlikely to be significant immediately after pipette break-in, when our major analyses of  $D_{\text{app}}^{\text{H}}$  were performed.

### Physiological relevance of low intrinsic $\text{H}^+$ mobility

Low effective intracellular  $\text{H}^+$  mobility has important implications for both the spatial and the temporal distribution of  $\text{pH}$  within a cardiac cell. Membrane transport of acid or base will set up a sub-membranous  $\text{pH}_i$  microdomain that extends by diffusion into the bulk cytoplasm. The amplitude and spatial spread of this microdomain will depend on  $D_{\text{app}}^{\text{H}}$  and the magnitude and spatial distribution of the acid–base transporters.

The present work shows that a localized acid influx of about  $10 \text{ mmol l}^{-1} \text{ min}^{-1}$  evokes longitudinal  $\text{pH}_i$  gradients of 0.2–0.4 units. This raises the possibility that sarcolemmal acid fluxes of similar magnitude, but spatially

distributed around the periphery of a myocyte (quantitatively equivalent to a major activation of sarcolemmal NHE; Leem *et al.* 1999) may generate radial gradients of p*H*<sub>i</sub> extending from the surface to the core of the myocyte, a distance of about 8 μm. It is notable that over similar distances in the nominal absence of CO<sub>2</sub>/HCO<sub>3</sub><sup>-</sup>, apical transport of acid into mammalian duodenal enterocytes generates acidic subapical microdomains (of Δp*H* 0.1–0.2 units) that last for several minutes (Stewart *et al.* 2000). However, given that NHE and other membrane acid transporters in the ventricular myocyte may be expressed in the t-system, as well as the sarcolemma (Petrecca *et al.* 1999), this will effectively reduce cytoplasmic diffusion distance to any given transport site, hence minimizing spatial p*H*<sub>i</sub> gradients. On the other hand, if NHE and other acid–base transporters communicated with subsarcolemmal, ‘fuzzy spaces’ with restricted passage for diffusion into the bulk cytoplasm, a low apparent diffusion coefficient for H<sup>+</sup> would readily result in major, transient p*H*<sub>i</sub> microdomains. High resolution imaging in cardiomyocytes will now be required to test the idea that significant p*H*<sub>i</sub> microdomains can be generated by sarcolemmal H<sup>+</sup> equivalent transport.

Finally, the low intrinsic  $D_{\text{app}}^{\text{H}}$  determined in the present work is quantitatively similar to the apparent diffusion coefficient for intracellular Ca<sup>2+</sup> determined recently in neurons ( $2 \times 10^{-7} \text{ cm}^2 \text{ s}^{-1}$ ; Gabso *et al.* 1997), cells where transient Ca<sup>2+</sup><sub>i</sub> microdomains are a common feature.

Further consideration of p*H*<sub>i</sub> microdomains is deferred until the Discussion of the accompanying paper (Spitzer *et al.* 2002), where we consider the facilitation of intracellular acid movement by CO<sub>2</sub>/HCO<sub>3</sub><sup>-</sup> and its regulation by carbonic anhydrase.

## APPENDIX

### Mathematical model for diffusion of H<sup>+</sup> ions or SNARF from a constant source

Two types of experiment were performed in order to estimate the apparent diffusion coefficient for H<sup>+</sup> ions. In the first, the pH-sensitive fluorophore carboxy-SNARF-1 was diffused into a myocyte in order to estimate its intracellular mobility. In the second, HCl was diffused, to estimate the effective mobility of intracellular H<sup>+</sup> as indicated by the SNARF fluorophore. In both cases estimates of mobility were made using the same mathematical model of diffusion. This assumes that solute (SNARF or H<sup>+</sup>) diffuses freely and continuously into the cell from the pipette and that it is neither buffered nor sequestered within the cell. For simplicity, diffusion is assumed to proceed in two dimensions only (along the length and the width of the cell). The dimensions of the cell are finite and the pipette is located close to one end of the

cell. The spatial and temporal characteristics of solute loading are reproduced by assuming an appropriate solute diffusion coefficient. In the case of the H<sup>+</sup> ion, this is the apparent intracellular diffusion coefficient,  $D_{\text{app}}^{\text{H}}$ . In Discussion we consider how  $D_{\text{app}}^{\text{H}}$  is related to the real buffer-mediated mechanism of H<sup>+</sup> movement within the cell.

### Numerics

The model was discretized using a Crank-Nicholson scheme for the diffusion term. The spatial dimensions for the domain of the model were chosen to agree with the cell dimensions. Placement of the source term was determined by the placement of the experimental pipette. A time step of 1 s was used for both sets of simulations (SNARF and H<sup>+</sup>). A space step of 1 μm was used for the H<sup>+</sup> ion simulations, and a space step of about 0.25 μm was used for the SNARF simulations, matching the resolution of data collection. The pipette width was taken to be  $l = 2 \text{ μm}$ .

### Comparison between experimental data and the model

**SNARF diffusion experiments.** For the SNARF experiment, fluorescence data corresponding to SNARF dye concentration were compared with their counterpart in the model. The model was fitted to spatial profiles at discrete times (for example see Fig. 4). Since the model is linear, the maximum SNARF concentration was assumed to occur at ROI 1 in the cell, and the model concentration at that point was scaled to equal the maximum concentration of dye measured in ROI 1 in the real experiment. The best fit diffusion coefficient was chosen using a least-squares error test. For each discrete time, each model data point in the spatial profile was subtracted from the corresponding experimental data point, squared and added together to give a measure of the error at that discrete time. Each of these errors was added together to give a measure of the error for the entire cell. An entire cell error value was found as a function of the diffusion coefficient, and the best fit diffusion coefficient was that value that minimized the entire cell error. The sensitivity of the spatial profiles to variations in the selected diffusion coefficient is shown in the inset in Fig. 4.

**H<sup>+</sup> diffusion experiments.** Fluorescence data corresponding to p*H*<sub>i</sub> were converted to H<sup>+</sup> ion concentration and were compared with their counterpart in the model. The model was fitted to time courses recorded at discrete spatial sites (ROIs; for example see Fig. 8). Since the model is linear, the model data were scaled to the experimental maximum [H<sup>+</sup>]<sub>i</sub> recorded in ROI 2. For each ROI, the time course was compared with the model. Each experimental concentration at a given time was compared with the model concentration at the nearest second. The difference was taken, squared and summed to provide a measure of error for the time series at that ROI. The sum of this error for

ROI 2 and ROI 3 for each cell was added, and the diffusion coefficient was chosen to minimize this total error.

### Derivation of the model

The basis for the model was the 2-dimensional diffusion equation with a constant source:

$$\frac{du}{dt} = D \frac{d^2u}{dx^2} + D \frac{d^2u}{dy^2} + \frac{1}{l^2} f\left(\frac{x}{l}, \frac{y}{l}\right), \quad (\text{A1})$$

where  $u(x,y,t)$  is the concentration of diffusing species, which is determined in space  $(x,y)$  and time  $(t)$ ,  $l$  is the width of the pipette, and  $f$  is defined as:

$$f(x,y) = \begin{cases} 1 & |x| < 0.5 \\ & |y| < 0.5 \\ 0 & \text{elsewhere} \end{cases}$$

The boundary conditions were no flux

$$\left. \frac{du}{dx} \right|_{x=a, x=b} = \left. \frac{du}{dy} \right|_{y=\pm L/2} = 0$$

where  $[a, b]$  and  $[-L/2, L/2]$  were the domain of the cell in the  $x$  and  $y$  directions, respectively (Fig. 12). In many of our experiments (e.g. Figs 3D and 7), the method for obtaining fluorescence data involved summing the pixel intensity in the width of a longitudinal measurement window. In these cases, the data were assumed to have no variation in  $y$  within the measurement window, even though the distribution of  $H^+$  or SNARF was not necessarily uniform in  $y$ . We therefore reduced the 2-dimensional diffusion model to a system of two one-dimensional diffusion equations in the length ( $x$ ), which allowed for incorporation of variations in the width ( $y$ ). These differential equations were solved numerically.

The solution of eqn (A1) with the given boundary conditions was represented as a Fourier cosine series in  $y$  so that:

$$u(x,y,t) = u_0(x,t) + \sum_{n=1}^{\infty} u_n(x,t) \cos\left(\frac{2n\pi y}{L}\right), \quad (\text{A2})$$

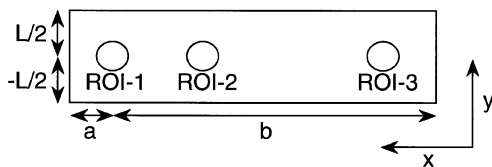


**Figure 12. Schematic diagram of myocyte used to model  $H^+$  and SNARF<sub>i</sub> diffusion**

The ROIs are illustrated along with the spatial domains of the cell in the  $x[a, b]$  and  $y[-L/2, L/2]$  directions. The pipette attachment site was at ROI 1.

where:

$$u_0(x,t) = \frac{1}{L} \int_{-L/2}^{L/2} u(x,y,t) dy,$$

and:

$$u_n(x,t) = \frac{2}{L} \int u(x,y,t) \cos\left(\frac{2n\pi y}{L}\right) dy.$$

Using the appropriate cosine projection onto eqn (A1) yielded:

$$\begin{aligned} \frac{1}{L} \int_{-L/2}^{L/2} \frac{du}{dt} \cos\left(\frac{2n\pi y}{L}\right) dy &= \frac{D}{L} \int_{-L/2}^{L/2} \frac{d^2u}{dx^2} \cos\left(\frac{2n\pi y}{L}\right) dy \\ &+ \frac{D}{L} \int_{-L/2}^{L/2} \frac{d^2u}{dy^2} \cos\left(\frac{2n\pi y}{L}\right) dy \\ &+ \frac{1}{L} \int_{-L/2}^{L/2} \frac{1}{l^2} f\left(\frac{x}{l}, \frac{y}{l}\right) \cos\left(\frac{2n\pi y}{L}\right) dy. \end{aligned}$$

Integrating by parts in the third integral and treating  $(1/l^2)f[(x/l), (y/l)]$  as a delta function in  $y$  while recalling the definition of  $u_0$  and  $u_n$  gave the following result:

$$\begin{aligned} \frac{du_0}{dt} &= D \frac{d^2u_0}{dx^2} + \frac{1}{Ll} f\left(\frac{x}{l}, 0\right), \\ \frac{du_n}{dt} &= D \left( \frac{d^2u_n}{dx^2} - \frac{4n^2\pi^2}{L^2} u_n \right) + \frac{2}{Ll} f\left(\frac{x}{l}, 0\right). \end{aligned}$$

The first two terms were assumed to provide a reasonable approximation to the sum in eqn (A2) yielding the two 1-dimensional diffusion equations:

$$\begin{aligned} \frac{du_0}{dt} &= D \frac{d^2u_0}{dx^2} + \frac{1}{Ll} f\left(\frac{x}{l}, 0\right), \\ \frac{du_1}{dt} &= D \left( \frac{d^2u_1}{dx^2} - \frac{4\pi^2}{L^2} u_1 \right) + \frac{2}{Ll} f\left(\frac{x}{l}, 0\right). \end{aligned}$$

The concentration of  $u$  was then approximated by:

$$u(x,y,t) \approx u_0(x,t) + \cos(2\pi y/L) u_1(x,t).$$

The longitudinal measurement window (width  $w = 5 \mu\text{m}$ ) used in the model was offset from the centre of the ROIs by  $2 \mu\text{m}$ . We approximated the measured data by:

$$U(x,t) = u_0(x,t) + s u_1(x,t),$$

where:

$$s = \frac{1}{w} \int_2^{w+2} \cos\left(\frac{2\pi y}{L}\right) dy.$$

For each cell, longitudinal profiles of  $[H^+]_i$  were computed for the first  $\sim 100$  s following pipette break-in using the cell dimensions, pipette location and an assumed maximum  $[H^+]_i$ . The trajectory of  $[H^+]_i$  at sites corresponding to the

measured ROIs were extracted from these data and statistically compared with the measured [H<sup>+</sup>]<sub>i</sub> trajectories as described above. Iterations of this process using varying values of maximum [H<sup>+</sup>]<sub>i</sub> yielded best-fit values of  $D_{app}^H$  for each cell.

## REFERENCES

- AL-BALDAWI, N. F. & ABERCROMBIE, R. F. (1992). Cytoplasmic hydrogen ion diffusion coefficient. *Biophysical Journal* **61**, 1470–1479.
- ALLEN, D. G., MORRIS, P. G., ORCHARD, C. H. & PIROLO, J. S. (1985). A nuclear magnetic study of metabolism in the ferret heart during hypoxia and inhibition of glycolysis. *Journal of Physiology* **361**, 185–204.
- ALLEN, D. G. & ORCHARD, C. H. (1987). Myocardial contractile function during ischemia and hypoxia. *Circulation Research* **60**, 153–168.
- BASSNETT, S., REINISCH, L. & BEBBE, D. C. (1990). Intracellular pH measurements using single excitation-dual emission fluorescence. *American Journal of Physiology* **258**, C171–178.
- BLANK, P. S., SILVERMAN, H. S., CHUNG, O. K. Y., HOGUE, B. A., STERN, M. D., HANSFORD, R. G., LAKATTA, E. G. & CAPOGROSSI, M. C. (1992). Cytosolic measurements in single cardiac myocytes using carboxy-seminaphthorhodafleur-1. *American Journal of Physiology* **263**, H276–284.
- BLATTER, L. A. & WIER, W. G. (1990). Intracellular diffusion, binding, and compartmentalization of the fluorescent calcium indicators indo-1 and fura-2. *Biophysical Journal* **58**, 1491–1499.
- BOUTRA, C. & VAUGHAN-JONES, R. D. (1989). Effects of intracellular and extracellular pH on contraction in isolated mammalian cardiac muscle. *Journal of Physiology* **418**, 163–187.
- BUCKLER, K. J. & VAUGHAN-JONES, R. D. (1990). Application of a new pH-sensitive fluoroprobe (carboxy-SNARF-1) for intracellular pH measurement in small, isolated cells. *Pflügers Archiv* **417**, 234–239.
- CH'EN, F. F., VAUGHAN-JONES, R. D., CLARKE, K. & NOBLE, D. (1998). Modelling myocardial ischaemia and reperfusion. *Progress in Biophysics and Molecular Biology* **69**, 515–538.
- CHACON, E., REECE, J. M., NIEMINEN, A. L., ZAHREBELSKI, G., HERMAN, B. & LEMASTERS, J. J. (1994). Distribution of electric potential, pH, free Ca<sup>2+</sup>, and volume inside cultured adult rabbit cardiac myocytes during chemical hypoxia: a multiparameter digitized confocal microscope study. *Biophysical Journal* **66**, 942–952.
- DONOSO, P., MILL, J. G., O'NEILL, S. C. & EISNER, D. A. (1992). Fluorescence measurements of cytoplasmic and mitochondrial sodium concentration in rat ventricular myocytes. *Journal of Physiology* **48**, 493–509.
- GABSO, M., NEHER, E. & SPIRA, M. E. (1997). Low mobility of the Ca<sup>2+</sup> buffers in axons of cultured Aplysia neurons. *Neuron* **18**, 473–481.
- GADIAN, D. G., RADDA, G. K., DAWSON, M. J. & DOUGLAS, R. W. (1982). pH<sub>i</sub> measurements of cardiac and skeletal muscle using <sup>31</sup>P-NMR. In *Intracellular pH: Its Measurement, Regulation, and Utilization in Cellular Functions*, pp. 61–77. Alan R. Liss, Inc., NY, USA.
- GONDA, T., MAOUYA, D., REES, S. E. & MONTROSE, M. H. (1999). Regulation of intracellular pH gradients by identified Na/H exchanger isoforms and a short-chain fatty acid. *American Journal of Physiology* **276**, G259–270.
- HARRISON, S. M., FRAMPTON, J. E., MCCALL, E. & ORCHARD, C. H. (1992). Contraction and intracellular Ca<sup>2+</sup>, Na<sup>+</sup> and H<sup>+</sup> during acidosis in rat ventricular myocytes. *American Journal of Physiology* **262**, C348–357.
- HAUGLAND, R. P. (1996). *Handbook of Fluorescent Probes and Research Chemicals*, 6th edn. Molecular Probes, Inc., Eugene, OR, USA.
- HOUSE, J. R., MILLER, D. J. & O'DOWD, J. J. (1989). Differences in the distribution of the imidazoles of rat heart between atria and ventricles. *Journal of Physiology* **417**, 162P.
- IMANAGA, I., KAMEYAMA, M. & IRISAWA, H. (1987). Cell-to-cell diffusion of fluorescent dyes in paired ventricular cells. *American Journal of Physiology* **252**, H223–232.
- IRVING, M., MAYLIE, J., SIZTO, N. L. & CHANDLER, W. K. (1990). Intracellular diffusion in the presence of mobile buffers. Application to proton movement in muscle. *Biophysical Journal* **57**, 717–721.
- JACOBUS, W. E., PORES, I. H., LUCAS, S. K., KALLMAN, C. H., WEISFELD, M. L. & FLAHERTY, J. T. (1982). The role of intracellular pH in the control of normal and ischemic myocardial contractility: a <sup>31</sup>P nuclear magnetic resonance and mass spectrometry study. In *Intracellular pH: Its Measurement, Regulation, and Utilization in Cellular Functions*, pp. 537–565. Alan R. Liss, Inc., NY, USA.
- JUNGE, W. & MCLAUGHLIN, S. (1987). The role of fixed and mobile buffers in the kinetics of proton movement. *Biochimica et Biophysica Acta* **890**, 1–5.
- KOHMOTO, O., SPITZER, K. W., MOVESEIAN, M. A. & BARRY, W. H. (1990). Effects of intracellular acidosis on [Ca<sup>2+</sup>]<sub>i</sub> transients, transsarcolemmal Ca<sup>2+</sup> fluxes, and contraction in ventricular myocytes. *Circulation Research* **66**, 622–632.
- KONISHI, M., OLSON, A., HOLLINGWORTH, S. & BAYLOR, S. M. (1988). Myoplasmic binding of fura-2 investigated by steady-state fluorescence and absorbance measurements. *Biophysical Journal* **54**, 1089–1104.
- LEEM, C. H., LAGADIC-GOSSMANN, D. & VAUGHAN-JONES, R. D. (1999). Characterization of intracellular pH regulation in the guinea-pig ventricular myocyte. *Journal of Physiology* **517**, 159–180.
- LIDE, D. R. (2001a). Properties of amino acids. In *CRC Handbook of Chemistry and Physics*, section 7, *Biochemistry*, 82nd edn, pp. 1–2. CRC Press, London.
- LIDE, D. R. (2001b). Dissociation constants of organic acids and bases. In *CRC Handbook of Chemistry and Physics*, section 8, *Analytical Chemistry*, 82nd edn, pp. 46–56. CRC Press, London.
- O'DOWD, J. J., ROBINS, D. J. & MILLER, D. J. (1988). Detection, characterization, and quantification of carnosine and other histidyl derivatives in cardiac and skeletal muscle. *Biochimica et Biophysica Acta* **967**, 241–249.
- ORCHARD, C. H. & CINGOLANI, H. E. (1994). Acidosis and arrhythmias in cardiac muscle. *Cardiovascular Research* **28**, 1312–1319.
- PETERSON, M. B., MEAD, R. J. & WELTY, J. D. (1973). Free amino acids in congestive heart failure. *Journal of Molecular and Cellular Cardiology* **5**, 139–147.
- PETRECCA, K., ATANASIU, R., GRINSTEIN, S., ORLOWSKI, J. & SHRIER, A. (1999). Subcellular localization of the Na<sup>+</sup>/H<sup>+</sup> exchanger NHE1 in rat myocardium. *American Journal of Physiology* **276**, H709–717.
- RANDALL, P. J. & TUBBS, P. K. (1979). Carbohydrate and fatty acid metabolism. In *Handbook of Physiology*, section 2, *The Cardiovascular System*, vol. I, *The Heart*, chap. 23, ed. BERNE, R. M., SPERELAKIS, N. & GEIGER, S. R., pp. 805–844. American Physiological Society, Bethesda, MD, USA.
- SKOLNICK, R. L., LITWIN, S. E., BARRY, W. H. & SPITZER, K. W. (1998). Effect of ANG II on pH<sub>i</sub>, [Ca<sup>2+</sup>]<sub>i</sub>, and contraction in rabbit ventricular myocytes from infarcted hearts. *American Journal of Physiology* **275**, H1788–1797.

- SPITZER, K. W. & BRIDGE, J. H. B. (1992). Relationship between intracellular pH and tension development in resting ventricular muscle and myocytes. *American Journal of Physiology* **262**, C316–327.
- SPITZER, K. W., ERSHLER, P. R., SKOLNICK, R. L. & VAUGHAN-JONES, R. D. (2000). Generation of intracellular pH gradients in single cardiac myocytes with a microperfusion system. *American Journal of Physiology – Heart and Circulatory Physiology* **278**, H1371–1382.
- SPITZER, K. W., SKOLNICK, R. L., PEERCY, B. E., KEENER, J. P. & VAUGHAN-JONES, R. D. (2002). Facilitation of intracellular H<sup>+</sup> ion mobility by CO<sub>2</sub>/HCO<sub>3</sub><sup>-</sup> in rabbit ventricular myocytes is regulated by carbonic anhydrase. *Journal of Physiology* **541**, 159–167.
- STEWART, A. K., BOYD, C. A. R. & VAUGHAN-JONES, R. D. (2000). A novel role for carbonic anhydrase: pH gradient dissipation in mouse small intestinal enterocytes. *Journal of Physiology* **516**, 209–217.
- SULEIMAN, M. S. & CHAPMAN, R. A. (1993). Changes in the principal free intracellular amino acids in the Langendorff perfused guinea pig heart during arrest with calcium-free or high potassium media. *Cardiovascular Research* **27**, 1810–1814.
- TAKIHARI, K., AZUMA, J., AWATA, N., OHTA, H., HAMAGUCHI, T., SAWAMURA, A., TANAKA, Y., KISHIMOTO, S. & SPERELAKIS, N. (1986). Beneficial effect of taurine in rabbits with chronic congestive heart failure. *American Heart Journal* **112**, 1278–1284.
- VANYSEK, P. (1999). Ionic conductivity and diffusion at infinite dilution. In *CRC Handbook of Chemistry and Physics*, 79th edn, section 5, *Thermochemistry, Electrochemistry and Kinetics*, ed. LIDE, D. R., pp. 93–95. CRC Press, London.
- VAUGHAN-JONES, R. D., EISNER, D. A. & LEDERER, W. J. (1987). Effects of intracellular pH on contraction in sheep cardiac Purkinje fibers. *Journal of General Physiology* **89**, 1015–1032.
- VAUGHAN-JONES, R. D., ERSHLER, P. R., SKOLNICK, R. L. & SPITZER, K. W. (2000a). Slow intracellular H<sup>+</sup> mobility regulated by carbonic anhydrase activity in rabbit ventricular myocytes. *Biophysical Journal* **78**, 223A.
- VAUGHAN-JONES, R. D., ERSCHLER, P., SKOLNICK, R. & SPITZER, K. W. (2000b). Intracellular H<sup>+</sup> mobility is facilitated by carbonic anhydrase activity in rabbit ventricular myocytes. *Journal of Physiology* **527.P**, 67P.
- WINDHOLZ, M., BUDAVARI, S., STROUMTSOS, L. Y. & FERTIG, M. N. (1976). *The Merck Index. An Encyclopedia of Chemicals and Drugs*. 9th edn, p.92. Merck & Co., Inc., Rahway, NJ, USA.
- ZHOU, Z. & NEHER, E. (1993). Mobile and immobile calcium buffers in bovine adrenal chromaffin cells. *Journal of Physiology* **469**, 245–273.

### Acknowledgements

This study was supported by grants from the British Heart Foundation and the Wellcome Trust to R.D.V.-J. and the National Heart, Lung, and Blood Institute (HL-42873) and the Nora Eccles Treadwell Foundation to K.W.S. We thank Dr P. R. Ershler for assistance with the confocal imaging. We also thank Dr David J. Miller for very useful discussion concerning intracellular histidine-linked dipeptides in heart.